NASA TECHNICAL NOTE

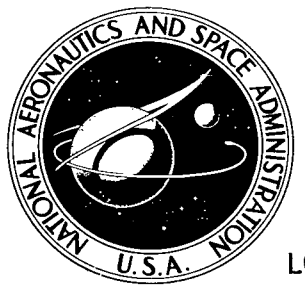

NASA TN D-4792

NASA TN D-4792

HEAT-TRANSFER AND PRESSURE DISTRIBUTIONS ON SPHERICALLY BLUNTED 25° HALF-ANGLE CONE AT MACH 8 AND ANGLES OF ATTACK UP TO 90°

by Dennis M. Bushnell, Robert A. Jones, and Jarrett K. Huffman

Langley Research Center
Langley Station, Hampton, Va.

NATIONAL AERONAUTICS AND SPACE ADMINISTRATION • WASHINGTON, D. C. • OCTOBER 1968

NASA TN D-4792

HEAT-TRANSFER AND PRESSURE DISTRIBUTIONS ON SPHERICALLY BLUNTED 25° HALF-ANGLE CONE AT MACH 8 AND ANGLES OF ATTACK UP TO 90°

By Dennis M. Bushnell, Robert A. Jones,
and Jarrett K. Huffman

Langley Research Center
Langley Station, Hampton, Va.

NATIONAL AERONAUTICS AND SPACE ADMINISTRATION

For sale by the Clearinghouse for Federal Scientific and Technical Information
Springfield, Virginia 22151 – CFSTI price $3.00

HEAT-TRANSFER AND PRESSURE DISTRIBUTIONS ON SPHERICALLY BLUNTED 25° HALF-ANGLE CONE AT MACH 8 AND ANGLES OF ATTACK UP TO 90°

By Dennis M. Bushnell, Robert A. Jones,
and Jarrett K. Huffman
Langley Research Center

SUMMARY

Local heat-transfer and pressure distributions have been measured over the conical portion of a spherically blunted 25° half-angle cone at angles of attack up to 90°. The investigation was conducted at a Mach number of 8.00 and Reynolds numbers of 0.37×10^6 and 1.65×10^6 based on free-stream conditions and model base diameter.

The pressure data are generally in good agreement with the semiempirical theory of Amick (NASA TN D-753) over the entire angle-of-attack range. The heat-transfer data for angles of attack up to 45° are in agreement with predictions using the small-cross-flow theory of Beckwith (NASA TR R-107); whereas, the data at higher angles of attack are fairly well represented by the swept-cylinder theory based on the local cone diameter.

INTRODUCTION

The cone has been the subject of numerous studies because it is a basic aerodynamic shape. The effects of such parameters as nose bluntness and angle of attack on heat-transfer and surface pressure distributions have been investigated at supersonic and hypersonic speeds. These investigations generally have been limited to cone half-angles of 15° or less. (For examples, see refs. 1 to 12.) Few heat-transfer data are available for angles of attack greater than the cone half-angle and for large half-angle cones.

Information concerning heat-transfer and pressure distributions about spherically blunted cones of large half-angle (greater than 15°) is of current interest because of the possible use of this type of configuration as a planetary entry vehicle. Small vehicles of this type will probably depend on aerodynamic stabilization, and the initial angle of attack could be large. Previous investigations of cones with large half-angle include the one reported in reference 11 where heat-transfer and pressure distributions obtained at a Mach number of 6.00 on a 20° half-angle cone up to an angle of attack of 15° were presented. Also, heat-transfer and pressure distributions over a 30° half-angle cone

obtained at a Mach number of 10.60 and up to an angle of attack of 20° are presented in reference 3, and pressure distributions over a spherically blunted 25° half-angle cone obtained at a Mach number of 20.00 and up to an angle of attack of 15° are presented in reference 13.

Several different semiempirical theories that predict the pressure distribution over a spherically blunted cone at angle of attack are available. Two of these theories are reported in references 9 and 14. These semiempirical methods give a fairly accurate prediction that can be used for engineering purposes. More exact theories for pressure distribution on sharp cones at angle of attack are available in references 15 and 16.

Two theoretical methods are presently available to predict the heat-transfer distribution over cones at angle of attack. One of these methods consists of the use of the local yawed-cylinder theory of reference 17 for the windward ray in conjunction with a Lees' heat-flux circumferential distribution. The other method is the use of a small-cross-flow theory such as reported in reference 18. Of the two methods, references 1 and 19 show that, for small cone angles and angles of attack less than 20°, the heat-transfer distributions predicted from the small-cross-flow theory are in better agreement with experimental data.

The purpose of this paper is to present measured pressure and heat-transfer distributions over a cone of 25° half-angle through an angle-of-attack range from 0° to 90°. The experimental pressure distributions are compared with predictions from several semiempirical theories; whereas, the experimental heat-transfer distributions are compared with predictions from small-cross-flow theory and local yawed-cylinder theory.

SYMBOLS

c_p specific heat

d model base diameter (fig. 1)

h heat-transfer coefficient

h_{sp} stagnation-point heat-transfer coefficient to sphere having radius r_N

M Mach number

p pressure

p_o' stagnation pressure behind a normal shock at free-stream conditions

R	Reynolds number
r_N	nose radius of model
s	distance along surface of model from zero-angle-of-attack stagnation point (fig. 1)
T	temperature
u	velocity in local streamwise direction
v	velocity normal to local streamwise direction
α	angle of attack
γ	specific-heat ratio
θ_c	cone half-angle
Λ	sweep angle
ϕ	roll angle, measured from windward ray

Subscripts:

aw	adiabatic wall
d	base diameter
e	local value external to boundary layer
eff	effective
es_t	transition value based on distance s
max	maximum value
sp	stagnation point

ϕ roll angle

∞ free stream

APPARATUS

Tunnel

The model tests were conducted in the Langley Mach 8 variable-density hypersonic tunnel. This tunnel is of the blowdown type and has an axially symmetric nozzle with contoured walls. For the present tests, the stagnation pressure was 165 psia (1.13 MN/m^2) and 915 psia (6.31 MN/m^2) with corresponding free-stream Mach numbers (see ref. 20) of 7.77 and 7.95. The corresponding values of stagnation temperature were 1285° R (714° K) and 1410° R (783° K). Values of free-stream Reynolds number $R_{\infty,d}$ based on the model base diameter of 5 inches (12.7 cm) were 0.37×10^6 and 1.65×10^6. Further information concerning this facility is available in reference 21.

Model and Instrumentation

A sketch of the model with instrumentation locations is shown in figure 1. The basic configuration is a spherically blunted 25° half-angle right circular cone with a base-diameter—nose-diameter ratio of 5. The nose section was solid and was not instrumented. The conical portion was rolled from 0.031-inch-thick (0.079-cm-thick) type 347 stainless steel. There were 2 rows of 30-gage (0.010-in. (0.025-cm) diameter) iron-constantan thermocouples having the same location s/r_N and installed 90° apart. The thermocouples were spotwelded to the inside surface of the model skin, with a 0.020-inch (0.051-cm) distance between the individual wires. A row of orifice tubes was located 180° from one of the thermocouple rows. The tubes had an inside diameter of 0.040 inch (0.102 cm) and were silver soldered flush with the model surface at the positions given in figure 1.

The temperature-time history of the model was recorded on magnetic tape with an analog-to-digital data-recorder system. The pressure data were recorded photographically from mercury manometers.

TEST PROCEDURES AND DATA REDUCTION

The heat-transfer data were obtained by a transient heating technique. For this technique, steady flow was established in the test section with the model outside the tunnel; then, the model was injected into the test-section flow for the test period. Heat-transfer data were obtained during the first few seconds after the model was in the tunnel

so that the model surface was still essentially isothermal at ambient temperature (80° F (300° K)). The heat-transfer tests were conducted at $R_{\infty,d} = 0.37 \times 10^6$ and 1.65×10^6. After a given test, the model was removed from the tunnel and cooled to an isothermal condition in preparation for another test. The time required to move the model through the tunnel boundary layer during injection was about 0.05 second, and care was taken to eliminate this effect from the data.

The temperature data were reduced to heating rates on a digital computing machine. Details of the data-reduction method used are available in reference 22. In order to obtain values of the heat-transfer coefficient, a recovery factor of 0.85 was assumed, where the recovery factor is defined as $\frac{T_{aw} - T_e}{T_{sp} - T_e}$. Curves faired through the pressure data were used to obtain values of p_e for the thermocouple locations where local pressures were not measured. For the calculation of T_e, an isentropic expansion from the model stagnation point to the local pressure level was assumed. The value of c_p used for the model material was 0.11 Btu/lbm-°R (460 J/kg-°K).

The pressure tests were conducted at $R_{\infty,d} = 1.65 \times 10^6$ only. The test time necessary to obtain the pressure data was of the order of 40 seconds to allow the mercury manometers to settle and, therefore, the pressure data were obtained with a model wall temperature considerably above room temperature. Circumferential distributions were obtained by rolling the model and repeating runs at essentially the same tunnel conditions.

ACCURACY

The accuracy of the heat-transfer data obtained by means of the automatic data-reduction system is a function of the level of the heating rates being measured. Because of errors in this data-reduction system and the possibility of additional errors in measured temperatures, skin thickness, and the values of density and specific heat of the material used, the estimated accuracy of the final heat-transfer-coefficient data is 15 percent. Conduction corrections due to the proximity of some thermocouples to the solid nose and base of the model are negligible.

The accuracy of the pressure data is determined primarily by the accuracy of the manometer data that can be read from the film. The percent error is a function of the pressure level being measured because the absolute reading error is about 0.010 inch (0.025 cm) of mercury. Because of these reading errors and also because of the possibility of errors in tunnel stagnation pressure, the maximum error in the final pressure data is about 3 percent for the windward surface measurements and 10 percent for the measurements on the lee side.

RESULTS AND DISCUSSION

Schlieren Photographs

As an aid in visualization of the flow about the model, schlieren photographs for the angle-of-attack range are given in figure 2. It is of interest to note (for $\alpha = 0^{o}$ to 15^{o}) the variations in shock-layer density and the inflection in shock shape just downstream of the nose that are caused by the overexpansion of the flow from the blunt nose. These phenomena are discussed in some detail in reference 3.

Pressure and Heat-Transfer Distributions for Zero Angle of attack

Pressure distribution.- The measured pressure data are shown in figure 3. Also shown are the predictions of the blunt-body theory of reference 23 for $M_{\infty} = 8.00$ and $\gamma = 1.4$. Good agreement is obtained between the present data and the theory. The characteristic overexpansion downstream of the shoulder is clearly evident. Both data and theory agree with the theoretical sharp-cone pressure level (ref. 24) for $s/r_N \geq 7$.

Heat-transfer distribution.- The heat-transfer data are shown plotted in figure 4 for both values of $R_{\infty,d}$. The measured coefficients have been nondimensionalized by the theoretical zero-angle-of-attack laminar stagnation-point values h_{sp}. For $R_{\infty,d} = 0.37 \times 10^{6}$, $h_{sp} = 0.014$ Btu/ft^2-sec-^{o}R (2.86×10^{2} W/m^2-^{o}K); and for $R_{\infty,d} = 1.65 \times 10^{6}$, $h_{sp} = 0.034$ Btu/ft^2-sec-^{o}R (6.94×10^{2} W/m^2-^{o}K). These values were calculated by the method of reference 25 with the assumption of a Newtonian velocity gradient. Also shown in figure 4 is the prediction of the local similarity theory of reference 26. The theoretical pressure distribution shown in figure 3 was used in this calculation, which is for laminar boundary-layer flow with the external entropy assumed constant. There is fairly good agreement between data and theory except for $s/r_N \geq 7$ for the lower Reynolds number data.

Approximate calculations indicate that, in the present case, the high entropy air processed by the essentially normal portion of the body bow shock is swallowed by the body boundary layer at both test Reynolds numbers, and, therefore, the boundary layer is subjected to a variable external entropy environment. The discrepancies at $s/r_N \geq 7$ may be due to effects of this variable entropy situation which causes a change in the local external flow properties and introduces external vorticity.

If the discrepancies are due to the variable entropy situation, the discrepancies should be less for the results at the higher test Reynolds number where the boundary layer is thinner and the external entropy more nearly constant. This expectation is somewhat borne out by the data, which, therefore, tend to support the supposition that

the deviation between theory and experiment for $s/r_N \geq 7$ may be due to variable entropy effects.

Pressure Distributions at Angle of Attack

Windward ray.- Shown in figure 5 are the pressure measurements obtained at several values of s/r_N on the windward ray of the cone plotted against angle of attack. Also shown are the predictions of several approximate theories. The simplest of these is the equivalent-cone approach, where the windward ray is assumed to have the same pressure level as a sharp cone having a half-angle equal to $\theta_c + \alpha$. The modified Newtonian expression was taken from reference 27. The Amick semiempirical theory was taken from reference 9; whereas, that of High and Blick is from reference 14. (The method of reference 14 was derived for sharp cones only.)

Comparison of the present results with these various approximations indicates that the Amick theory best represents the data over the entire angle-of-attack range. Because the theory is semiempirical and was derived from data obtained on 5^o and 15^o half-angle sharp and blunt cones at Mach 3.86, the successful extrapolation to the conditions of the present tests implies a fairly general validity for the Amick expression.

Circumferential distributions.- Shown in figure 6 are the measured circumferential pressure distributions, along with the predictions of the same theories discussed in connection with figure 5. Again, the Amick theory (ref. 9) best represents the data over the entire angle-of-attack range. The fact that the circumferential predictions as well as the windward-ray predictions of this semiempirical theory were successful at the present test conditions (which were, as mentioned previously, much different from the conditions used to derive the theory) indicates that the theory is applicable to a wide range of cone angles, angles of attack, and free-stream conditions.

Heat-Transfer Distributions at Angle of Attack

Angles of attack of 75^o and 90^o.- The windward-ray heat-transfer distribution for angles of attack of 75^o and 90^o are shown in figures 7 and 8, respectively. The reference values of h_{sp} were computed in the same way indicated previously. Also shown is the prediction based on swept-cylinder stagnation-line theory for laminar boundary layers (ref. 17). In this calculation, the local diameter, as measured in a plane normal to the axis of the cone, was substituted for the cylinder diameter. The pressure level was obtained from the assumptions that the local shock was parallel to the surface of the windward ray (fig. 2), and that the sweep angle was given by the inclination of the windward ray. Except for end effects which are present for $s/r_N \geq 7$ and blunt-nose effects for $s/r_N \leq 3$, this simplified procedure seems to give a fair indication of the heat transfer.

The end effects are a result of the fact that the actual flow over the cone at these high angles of attack is in the negative s-direction. Therefore, initially, the heat transfer decreases as the boundary layer thickens in the negative s-direction. However, as the diameter decreases and the chordwise velocity gradients increase, the flow evidently assumed the nature of swept-cylinder-type flow corresponding to the local diameter. The characteristics of these end effects would presumably change depending on whether the base lip was sharp, as in the present case, or blunted. The blunt-nose effects, referred to previously are probably caused by the increased local sweep of the shock with respect to the free-stream flow as the nose is approached. This increased sweep is evident in figure 2 for $\alpha = 75^{\circ}$, and the effect would be to reduce local pressures and, therefore, heating rates below the predicted values for the simulated local swept cylinder would result.

The circumferential distributions for these large angles of attack are shown plotted in figures 9 and 10. The distribution is shown for the plane normal to the axis of the cone. The data have been divided by the measured value at $\phi \leqq 0^{\circ}$ for the same station s/r_N and Reynolds number. The theoretical distribution was computed by the method of reference 26 for flow around a swept cylinder where the local sweep angle and stagnation-line pressure level were computed from the assumptions previously mentioned.

Two pressure distributions corresponding to the theoretical curves shown in figure 6(b) were used in the calculations. Figures 9 and 10 indicate that this simple theory, which does not account for any cross-flow effects, predicts the heat-transfer distribution over the windward surface fairly well. The calculation using the Amick pressure distribution is, except for $\phi \leqq 30^{\circ}$, in somewhat better agreement with the data. This result can perhaps be expected because figure 6(b) shows the Amick theory to be in better agreement with the pressure data.

Angles of attack of 5° to 60°.- The heat-transfer distribution along the most windward surface of the cone for angles of attack of 5° to 60° and various circumferential roll angles are shown in figures 11 to 16. Also shown is the prediction of laminar small-cross-flow theory (ref. 18).

In the application of small-cross-flow theory, the location of the local inviscid streamlines and the pressure distribution along them must be known. In the present case, these quantities were computed by using the procedure outlined in reference 19 and, as in reference 19, the surface streamlines were calculated by the method of reference 28 by using polynomial curve fits of the measured pressure distributions over the conical portion. Because pressures were not measured over the spherical nose portion, a modified Newtonian distribution was assumed and was faired through the measured values downstream of the tangency point. It was assumed that the flow expanded from the stagnation point with normal shock entropy. The curve fits of $p/p_{o'}$ as a function of ϕ,

obtained in the present procedure, are least accurate in the vicinity of $\phi = 0^{\circ}$; hence, the heat-transfer predictions shown for $\phi = 0^{\circ}$ were actually those computed for values of ϕ from 8° to 10°. However, these values should not differ by more than a few percent from the values for $\phi = 0^{\circ}$, and, therefore, are considered to be sufficiently accurate indications of the case where $\phi = 0^{\circ}$. The lee side of the cone at angle of attack is usually subjected to a separated and vortex-type flow for which the small-cross-flow theory would not be applicable.

For the lower Reynolds number (0.37×10^6), the agreement between experiment and theory is fairly good (except for $\alpha = 45^{\circ}$, $\phi = 0^{\circ}$ and 30°, and $s/r_N > 7$) up to an angle of attack of 45° (part (a) of figs. 11 to 15). The calculations for the small-cross-flow theory at $\alpha = 60^{\circ}$ (fig. 16) were continued beyond the end of the theoretical curves shown; however, the results were not plotted as they continue to diverge from the data. Disagreement begins to occur at $\alpha = 45^{\circ}$ and is very much in evidence at $\alpha = 60^{\circ}$ because at large α ($\alpha > 20^{\circ}$, where the sonic line has moved off the spherical portion of the nose), the assumption of a Newtonian stagnation-point location is probably not correct and, therefore, the calculations of the streamline locations and starting points are in error. If the correct streamline location could be computed (which would involve very detailed pressure measurements not available in the present case), the small-cross-flow theory might give good results, even at $\alpha = 60^{\circ}$, where the predictions in the present case are poor. In summary, even though the streamline calculations may be in error because of the possibility of an incorrect assumption concerning the location of the stagnation point, the small-cross-flow theory is seen to be useful for making engineering predictions of the heat-transfer distribution up to $\alpha = 45^{\circ}$, except for $s/r_N > 7$.

It is of interest to ascertain whether the main assumption of the small-cross-flow theory $(v/u)_{max} << 1$ has been violated in the region where agreement occurred ($\alpha \leq 45^{\circ}$). In reference 19, at an angle of attack of 18° on a 13.33° half-angle cone the ratio $(v/u)_{max}$ was estimated to have a maximum value of 4; however, this good agreement observed between theory and data indicated that the small-cross-flow theory may be useful even in cases where $(v/u)_{max}$ is not only much less than 1, but actually greater than 1. Estimations of the ratio $(v/u)_{max}$ for $\alpha = 45^{\circ}$ and 60° indicates a value of approximately 3 and 4, respectively. Therefore, disagreement at $\alpha = 60^{\circ}$ as well as at 45° for $s/r_N > 7$ is probably, as previously stated, due to a breakdown in the streamline calculation procedure rather than due to shortcomings of the small-cross-flow theory.

Also, the use of swept-cylinder theory would not adequately predict the windward-ray ($\phi = 0^{\circ}$) level for $\alpha = 60^{\circ}$ as can be seen by comparing the level of the data shown for $\phi = 0^{\circ}$ in figure 16(a) with the theoretical stagnation-line swept-cylinder level. The

swept-cylinder theory underpredicts the data for $\alpha = 60^{\circ}$ by about 25 percent. However, in general, the prediction is better than that of the small-cross-flow theory as presently applied. Because the effective sweep angle $\Lambda_{eff} = |90 - \theta_c - \alpha| = |65 - \alpha|$, $\Lambda_{eff} = 5^{\circ}$ at $\alpha = 60^{\circ}$; whereas, $\Lambda_{eff} = 10^{\circ}$ at $\alpha = 75^{\circ}$. There is poorer agreement of the swept-cylinder theory at $\alpha = 60^{\circ}$ (fig. 16) as compared with that at $\alpha = 75^{\circ}$ (fig. 7). One possible reason for the disagreement is that the flow is in the negative s-direction for $\alpha = 75^{\circ}$ and positive s-direction for $\alpha = 60^{\circ}$. Thus, the geometric end conditions are different for the two cases, but probably of more importance; the increasing values of local effective cylinder diameter in the flow direction for $\alpha = 60^{\circ}$ would reduce the stagnation-line boundary-layer thickness as compared to the case where $\alpha = 75^{\circ}$. This reduced boundary-layer thickness would in turn cause the higher heating rates relative to the theoretical values observed for $\alpha = 60^{\circ}$ than for $\alpha = 75^{\circ}$.

For the higher Reynolds number (1.65×10^6) tests, the agreement between the theoretical and experimental distributions was also generally good up to an angle of attack of 45° (part (b) of figs. 11 to 15) except at angles of attack of 10° and 15° and $s/r_N \geq 7$, where a marked disagreement between experiment and theory occurred (except for $\phi = 90^{\circ}$). This disagreement is probably due to transition, which seemed to occur at smaller s/r_N for small ϕ (less than 30°) than for large ϕ. The data for the lee side, which is presented subsequently, indicated that transition did not occur on the lee side. This tendency for transition to occur first on the windward surface is opposite to the trend shown in reference 2 where transition occurred first on the lee side. However, the tests in reference 2 were for a 13.33° half-angle sphere cone, and transition locations are given for $\alpha = 18^{\circ}$, where the lee surface is subjected to vortical flow, which may prematurely trip transition. In the present case, transition occurs for $\alpha = 10^{\circ}$ and 15° (fig. 12(b) and fig. 13(b), respectively) where the lee surface of the cone still "sees" the air flow, and, therefore, the vortical flow is probably not yet present. The variation of local-unit Reynolds number calculated for the windward ray of the cone (result is shown in fig. 17 where expansion from the stagnation point was assumed), indicated that where transition occurred (at $\alpha = 10^{\circ}$ and 15°) the local-unit Reynolds number is larger than for the other angles of attack in the test range.

The measured heat-transfer data are plotted against the circumferential angle ϕ in figure 18. This figure is included to make all the data available in a unified form, and, in particular, for $\phi > 90^{\circ}$ where no data have as yet been shown except for $\alpha = 75^{\circ}$ and 90° (figs. 9 and 10, respectively). The effect of vortical-type flow, referred to previously, is clearly apparent from the peak in heating at $\phi = 180^{\circ}$ for $\alpha \geq 30^{\circ}$ (figs. 18(i) to 18(l)).

CONCLUSIONS

Local heat-transfer rates and pressures have been measured over the conical portion of a spherically blunted 25° half-angle cone at angles of attack up to 90°. The model was tested at a Mach number of approximately 8.00 and Reynolds numbers of 0.37×10^6 and 1.65×10^6 based on free-stream conditions and model base diameter. The results of the investigation indicated the following conclusions:

1. The pressure data are generally in good agreement with the semiempirical theory of Amick (NASA TN D-753) over the entire angle-of-attack range.

2. The heat-transfer distributions over the windward surface for angles of attack up to 45° are in good agreement with predictions using the small-cross-flow theory of Beckwith (NASA TR R-107); whereas, the distributions at higher angles of attack are in fair agreement with swept-cylinder theory based on the local diameter of the cone.

3. Boundary-layer transition was observed at angles of attack of 10° and 15° for the high Reynolds number (1.65×10^6) tests on the windward surface only.

4. The leeward heat-transfer distributions for an angle of attack equal to or greater than 30° showed evidence (local peak in heating at most leeward ray) of a vortical type of flow.

Langley Research Center,
National Aeronautics and Space Administration,
Langley Station, Hampton, Va., May 22, 1968,
129-01-08-38-23.

REFERENCES

1. Conti, Raul J.: Laminar Heat-Transfer and Pressure Measurements at a Mach Number of 6 on Sharp and Blunt 15° Half-Angle Cones at Angles of Attack up to 90°. NASA TN D-962, 1961.

2. Pasiuk, Lionel: Supersonic Aerodynamic Heat Transfer and Pressure Distributions on a Sphere-Cone Model at High Angles of Yaw. NOLTR 62-35, U.S. Navy, July 1962.

3. Cleary, Joseph W.: Effects of Angle of Attack and Nose Bluntness on the Hypersonic Flow Over Cones. AIAA Paper No. 66-414, June 1966.

4. Tracy, Richard R.: Hypersonic Flow over a Yawed Circular Cone. Hypersonic Res. Proj. Mem. No. 69 (Contract No. DA-31-124-ARO(D)-33), Graduate Aeronaut. Lab., California Inst. Technol., Aug. 1, 1963.

5. Burke, G. L.: Heat Transfer and Pressure Distributions About Sharp and Blunt Elliptic Cones at Angles of Attack and High Mach Numbers. AFFDL-TR-64-172, U.S. Air Force, May 1965. (Available from DDC as AD465939.)

6. Lewis, Clark H., and Knox, Eugene C.: A Spherically Blunted Cone at Angle of Attack. AIAA J., vol. 4, no. 6, June 1966, pp. 1110-1111.

7. Wittliff, Charles E.; and Wilson, Merle R.: Heat Transfer to Slender Cones in Hypersonic Air Flow, Including Effects of Yaw and Nose Bluntness. Jour. Aerosp. Sci., vol. 29, no. 7, July 1962, pp. 761-774.

8. Rhudy, J. P.; Hiers, R. S.; and Rippey, J. O.: Investigation of Hypersonic Flow Over Blunted Plates and Cone. AEDC-TN-60-93, U.S. Air Force, May 1960.

9. Amick, James L.: Pressure Measurements on Sharp and Blunt 5°- and 15°-Half-Angle Cones at Mach Number 3.86 and Angles of Attack to 100°. NASA TN D-753, 1961.

10. Peckham, D. H.: Experiments at Hypersonic Speeds on Circular Cones at Incidence. Tech. Note No. Aero. 2863, Brit. R.A.E., Jan. 1963.

11. Zakkay, Victor: Pressure and Laminar Heat Transfer Results in Three-Dimensional Hypersonic Flow. WADC Tech. Note 58-182, ASTIA Doc. No. AD 155679, U.S. Air Force, Sept. 1958.

12. Julius, Jerome D.: Measurements of Pressure and Local Heat Transfer on a 20° Cone at Angles of Attack up to 20° for a Mach Number of 4.95. NASA TN D-179, 1959.

13. Harris, Julius E.: Aerodynamic Characteristics of a Spherically Blunted 25° Cone at a Mach Number of 20. NASA TN D-4098, 1967.

14. High, M. D.; and Blick, E. F.: Cone Pressure Distribution at Large and Small Angles of Attack. AIAA J., vol. 2, no. 11, Nov. 1964, pp. 2054-2055.

15. Eastman, D. W.; and Omar, M. E.: Flow Fields about Highly Yawed Cones by the Inverse Method. AIAA J., vol. 3, no. 9, Sept. 1965, pp. 1782-1784.

16. Moretti, Gino: Inviscid Flowfield About a Pointed Cone at an Angle of Attack. AIAA J., vol. 5, no. 4, Apr. 1967, pp. 789-791.

17. Beckwith, Ivan E.; and Gallagher, James J.: Local Heat Transfer and Recovery Temperatures on a Yawed Cylinder at a Mach Number of 4.15 and High Reynolds Numbers. NASA TR R-104, 1961.

18. Beckwith, Ivan E.: Similarity Solutions for Small Cross Flows in Laminar Compressible Boundary Layers. NASA TR R-107, 1961.

19. Pasiuk, Lionel: Comparisons of Experimental and Theoretical Heat Transfer to a Yawed Sphere-Cone Model at Supersonic Speeds. NOLTR 63-208, U.S. Navy, Oct. 1964.

20. Stainback, P. Calvin: Heat-Transfer Measurements at a Mach Number of 8 in the Vicinity of a 90° Interior Corner Alined With the Free-Stream Velocity. NASA TN D-2417, 1964.

21. Schaefer, William T., Jr.: Characteristics of Major Active Wind Tunnels at the Langley Research Center. NASA TM X-1130, 1965.

22. Stainback, P. Calvin: Heat-Transfer Measurements at a Mach Number of 4.95 on Two 60° Swept Delta Wings With Blunt Leading Edges and Dihedral Angles of 0° and 45°. NASA TN D-549, 1961.

23. Lomax, Harvard; and Inouye, Mamoru: Numerical Analysis of Flow Properties About Blunt Bodies Moving at Supersonic Speeds in an Equilibrium Gas. NASA TR R-204, 1964.

24. Sims, Joseph L.: Tables for Supersonic Flow Around Right Circular Cones at Zero Angle of Attack. NASA SP-3004, 1964.

25. Reshotko, Eli; and Cohen, Clarence B.: Heat Transfer at the Forward Stagnation Point of Blunt Bodies. NACA TN 3513, 1955.

26. Beckwith, Ivan E.; and Cohen, Nathaniel B.: Application of Similar Solutions to Calculation of Laminar Heat Transfer on Bodies With Yaw and Large Pressure Gradient in High-Speed Flow. NASA TN D-625, 1961.

27. Rainey, Robert W.: Working Charts for Rapid Prediction of Force and Pressure Coefficients on Arbitrary Bodies of Revolution by Use of Newtonian Concepts. NASA TN D-176, 1959.

28. Harris, E. L.: Determination of the Streamlines on a Sphere-Cone at Angle of Attack From the Measured Surface Pressure Distribution. NOLTR 63-37, U.S. Navy, Mar. 1963.

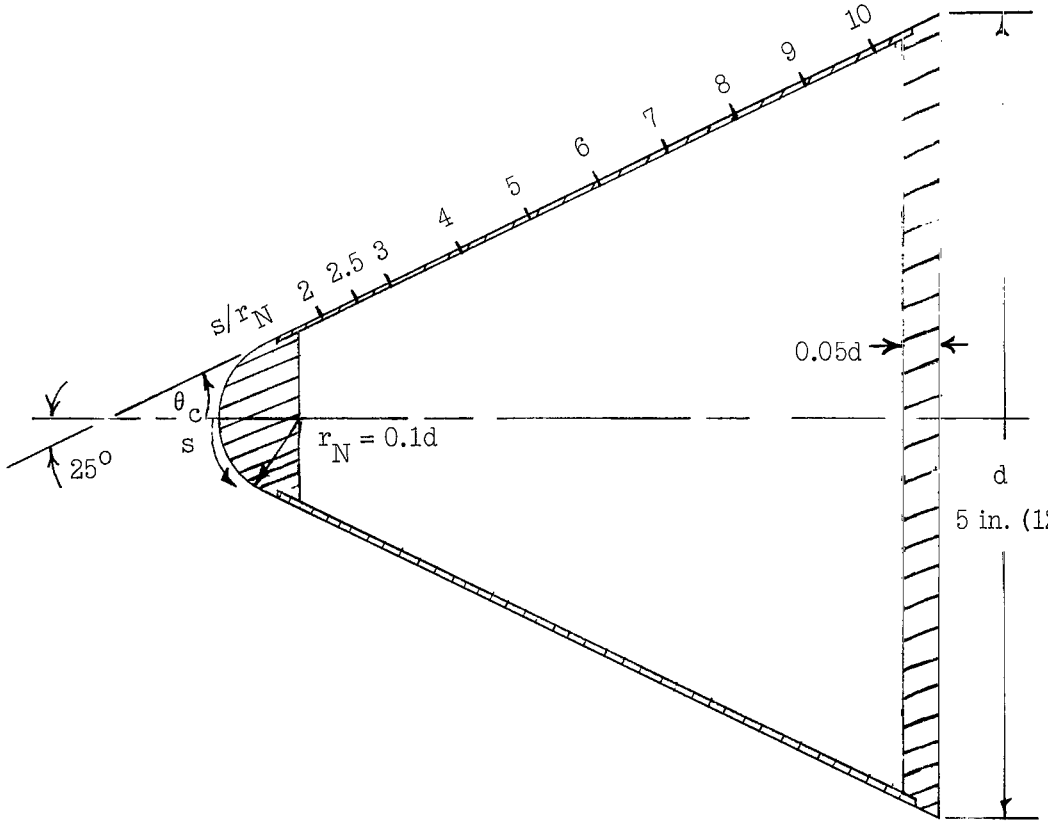

Instrumentation locations, s/r_N

Orifice	Thermocouple
2	2
2.5	2.5
3	3
5	4
7	5
9	6
	7
	8
	9
	10

Figure 1.- Model with instrumentation locations.

$\alpha = 0°$ $\alpha = 5°$ $\alpha = 10°$

$\alpha = 15°$ $\alpha = 30°$ $\alpha = 45°$

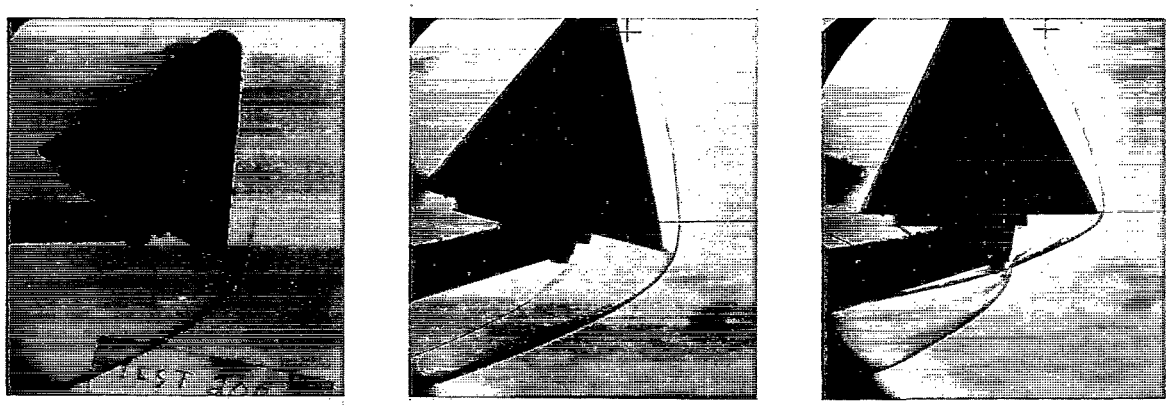

$\alpha = 60°$ $\alpha = 75°$ $\alpha = 90°$

Figure 2.- Schlieren photographs of flow field for angle-of-attack range. $R_{\infty,d} = 1.65 \times 10^6$. L-68-900

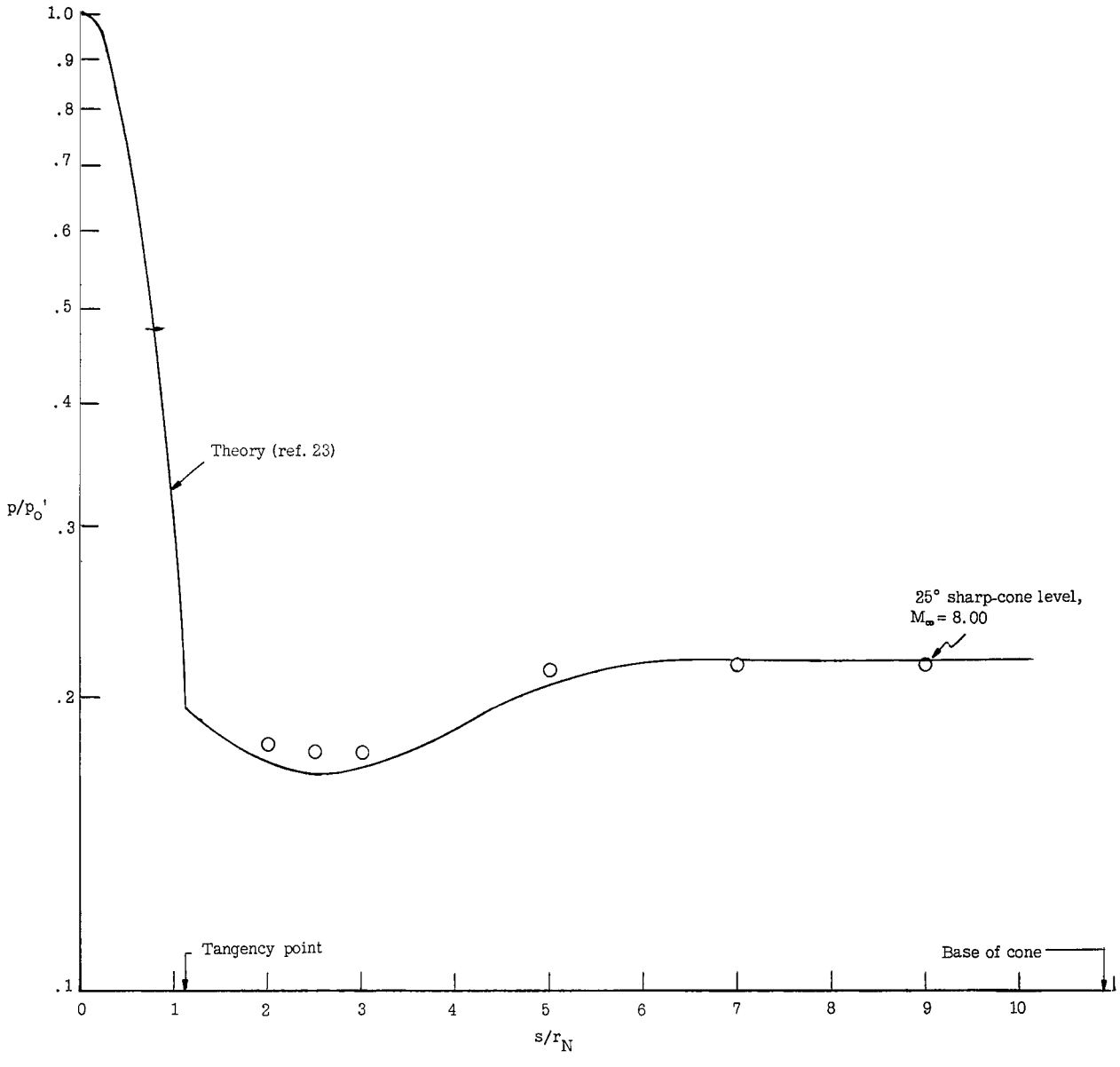

Figure 3.- Pressure distribution. Zero angle of attack; $R_{\infty,d} = 1.65 \times 10^6$.

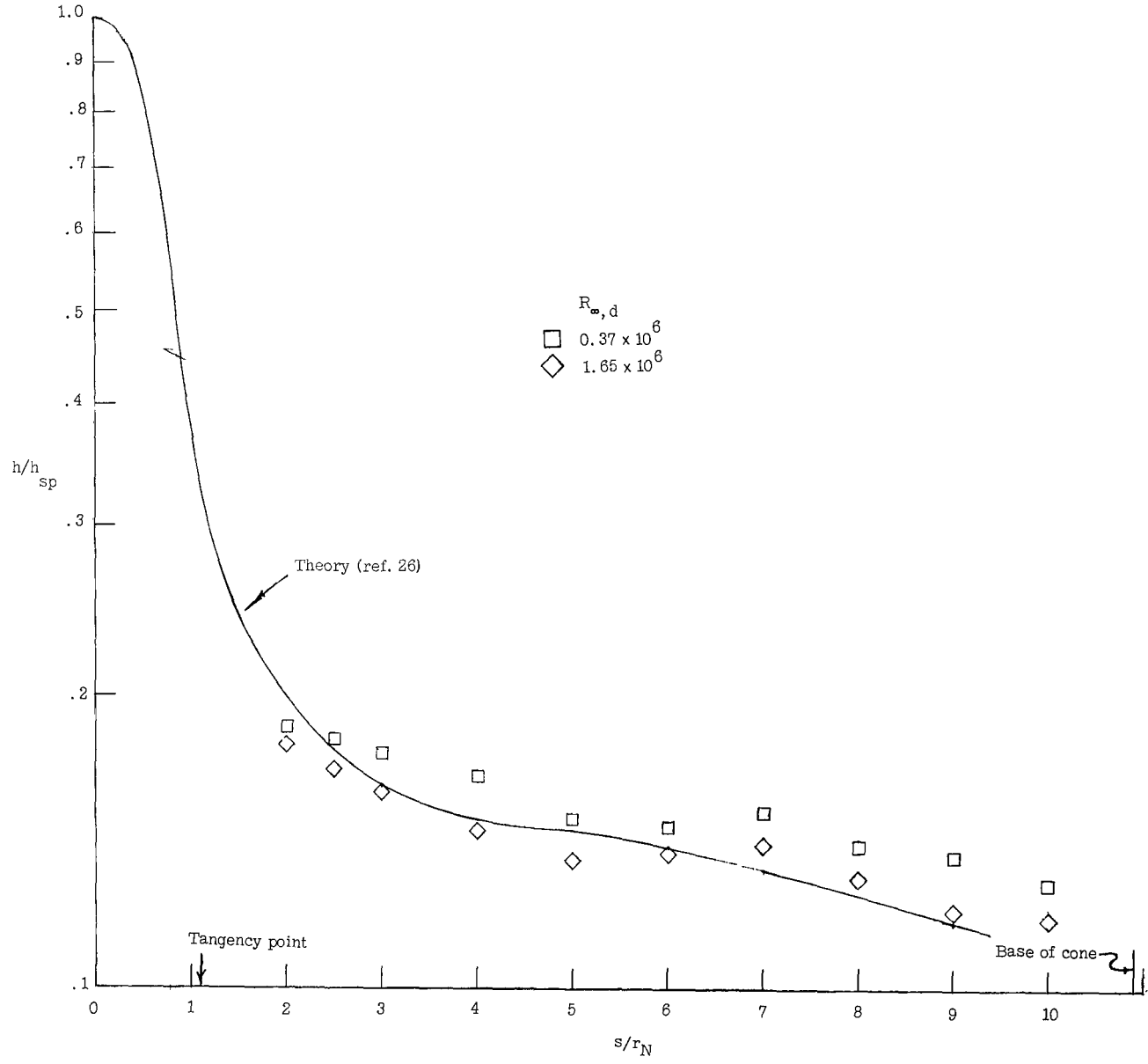

Figure 4.- Heat-transfer distribution. Zero angle of attack.

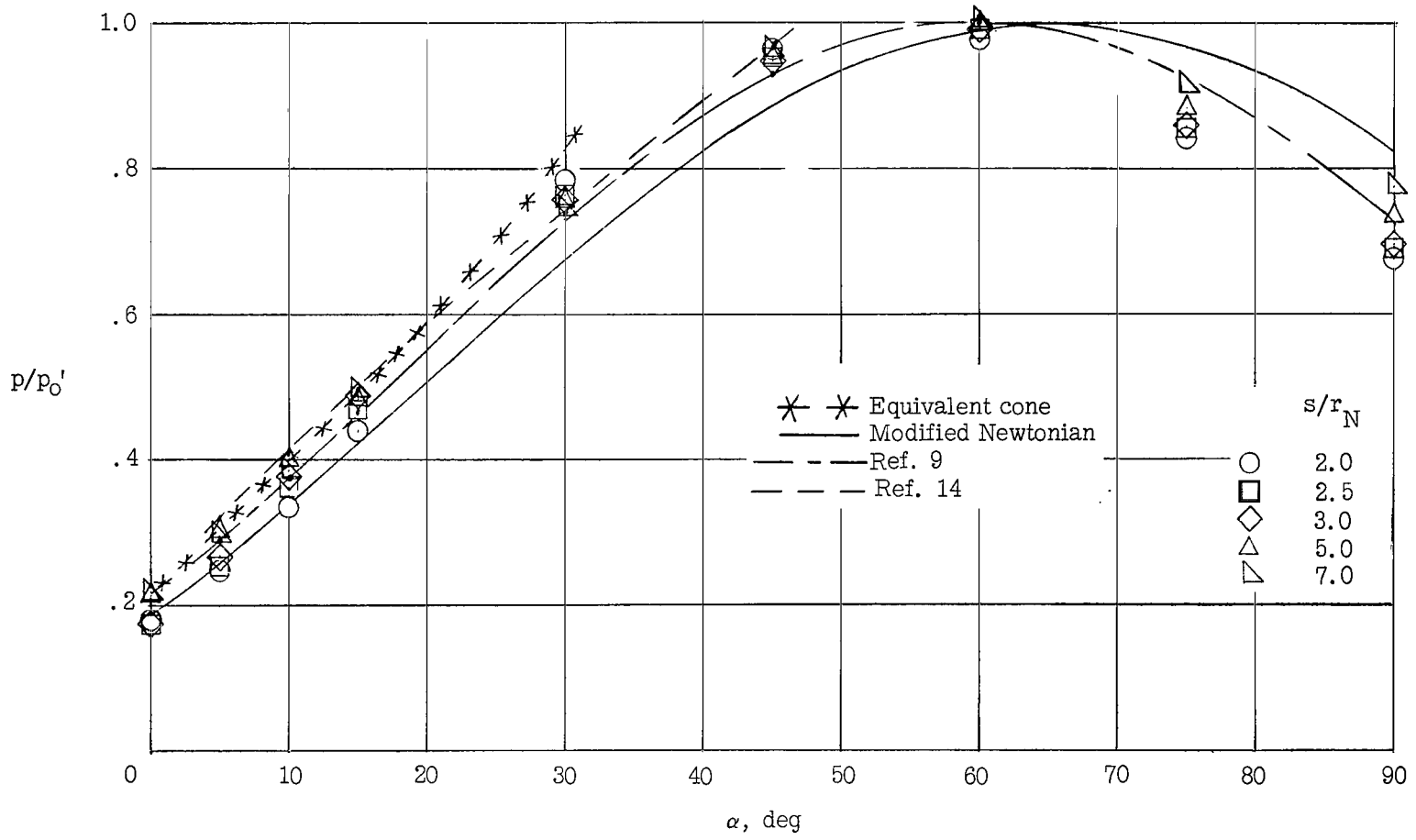

Figure 5.- Windward-ray pressure-level variation with angle of attack. $R_{\infty,d} = 1.65 \times 10^6$.

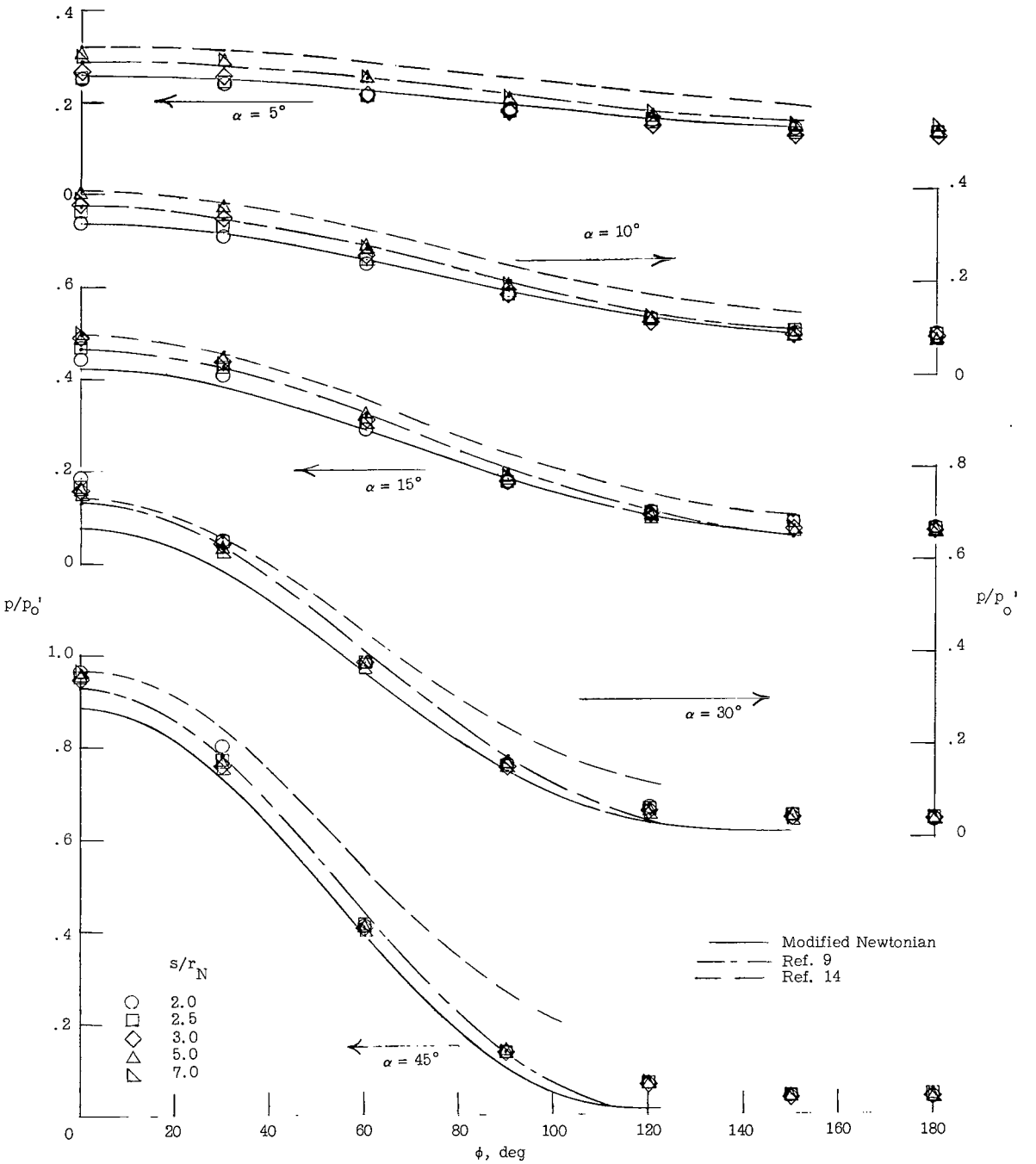

(a) $5^0 \leq \alpha \leq 45^0$.

Figure 6.- Circumferential pressure distributions. $R_{\infty,d} \leq 1.65 \times 10^6$.

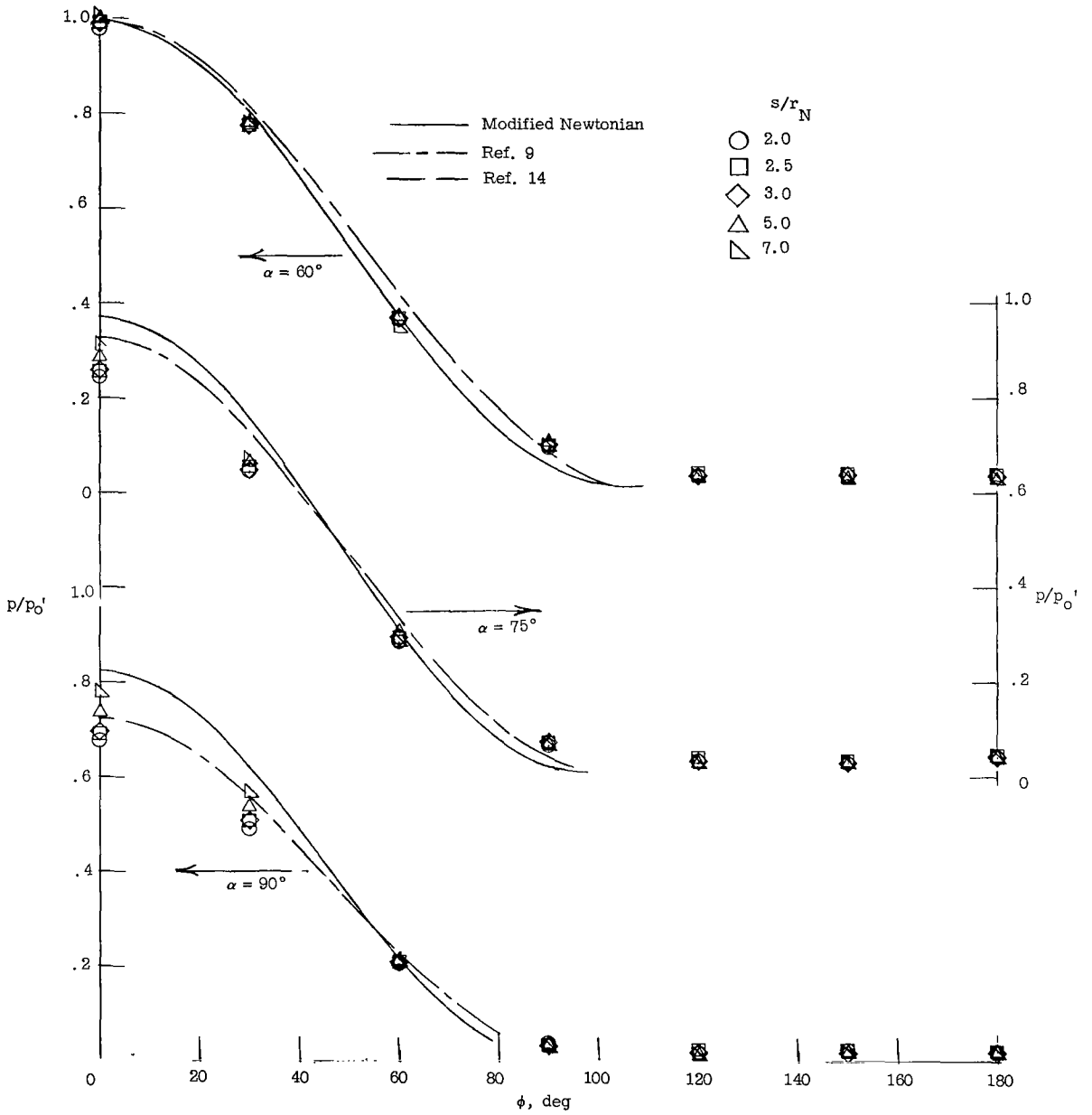

(b) $60^0 \leq \alpha \leq 90^0$.

Figure 6.- Concluded.

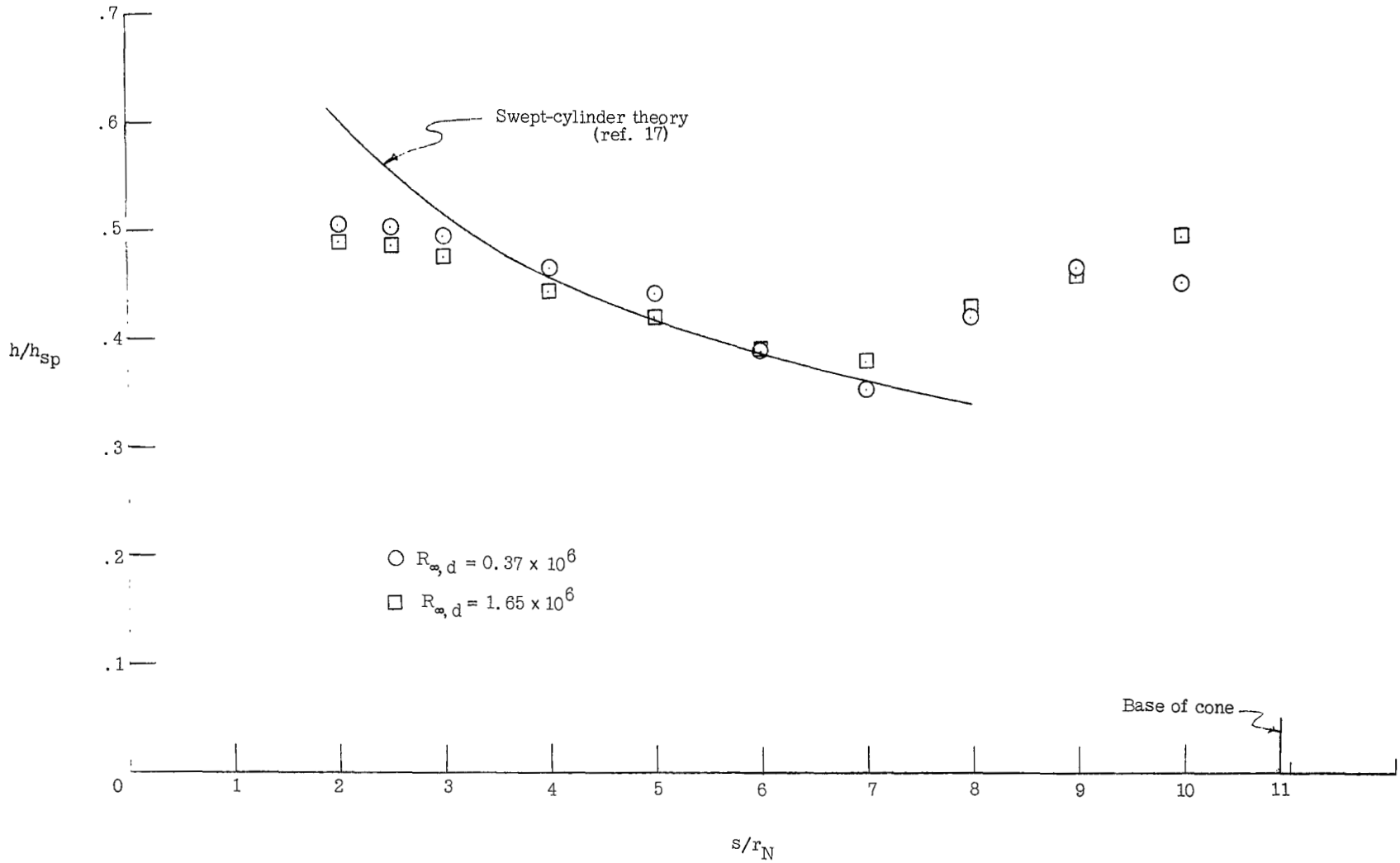

Figure 7.- Windward-ray heat-transfer distribution. $\alpha = 75^0$.

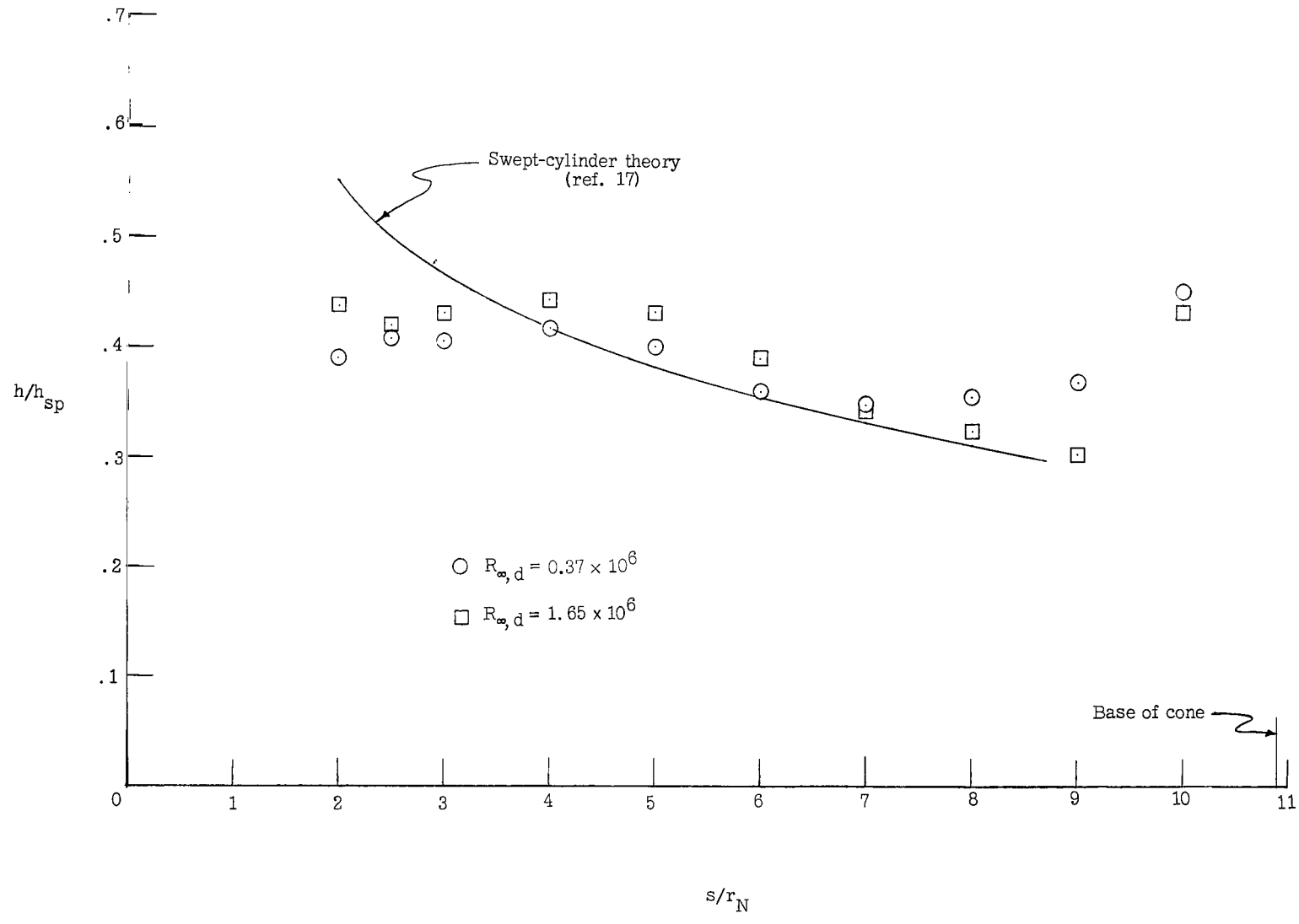

Figure 8.- Windward-ray heat-transfer distribution. $\alpha = 90^0$.

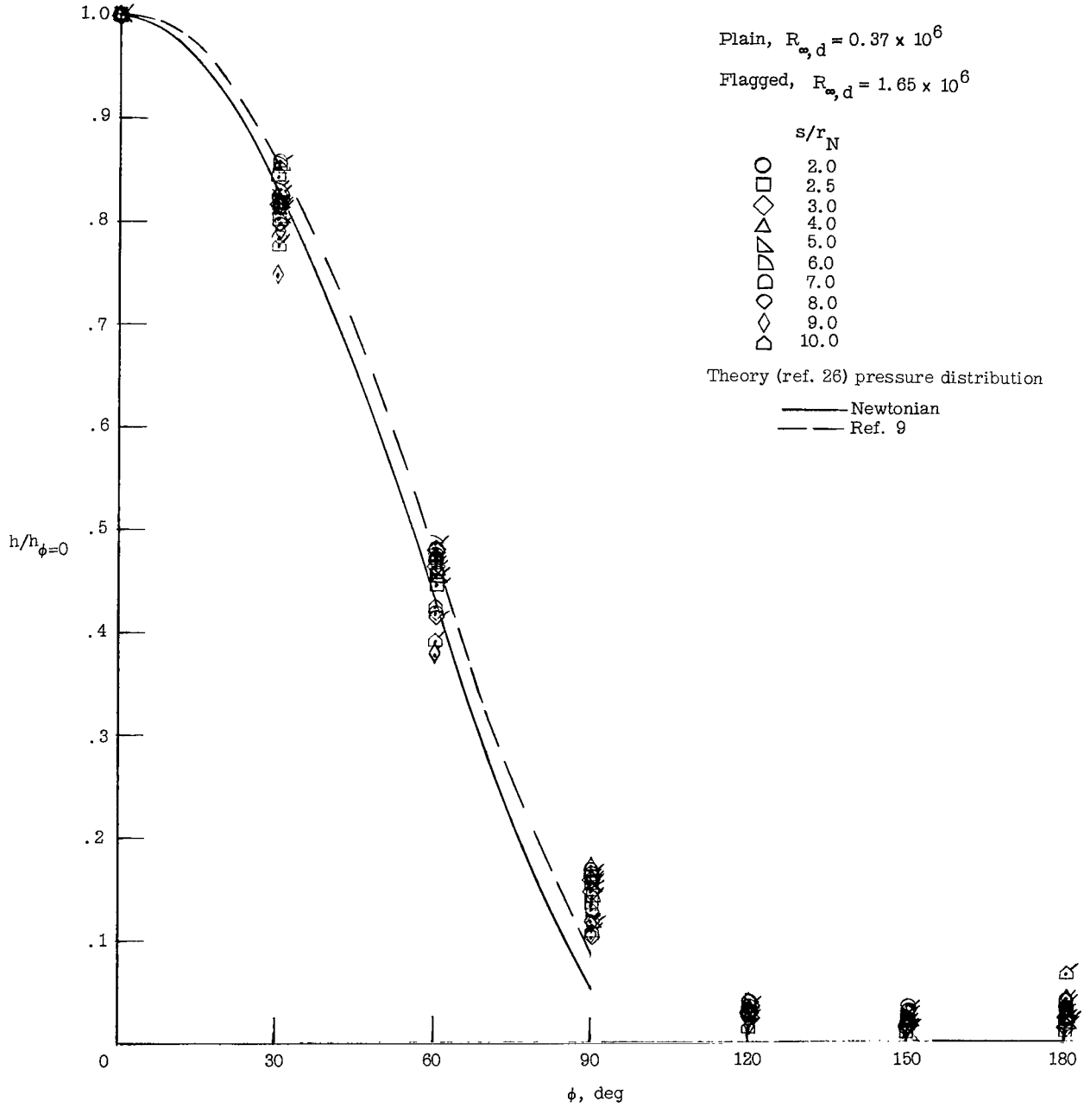

Figure 9.- Circumferential heat-transfer distribution. $\alpha = 75^0$.

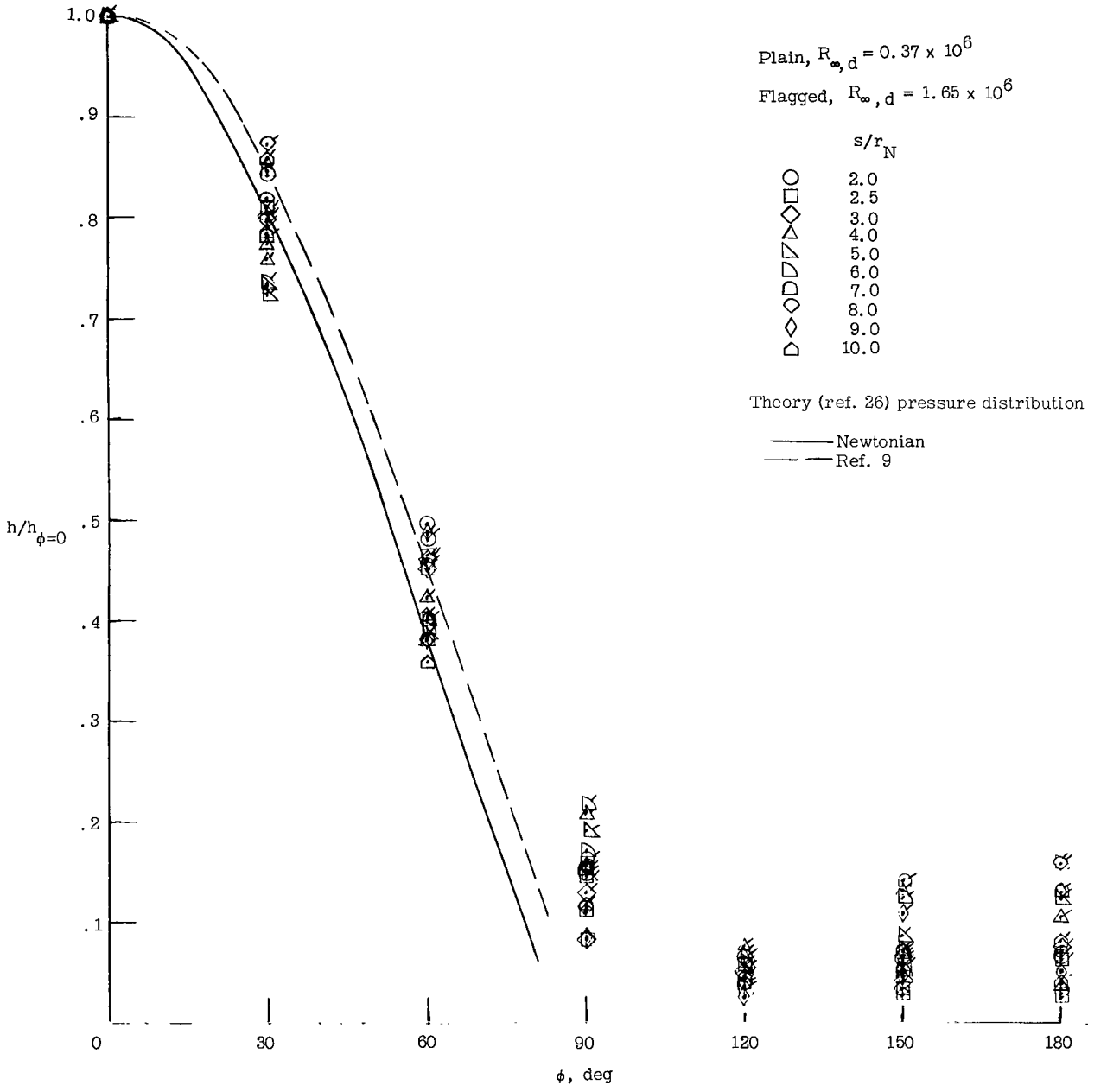

Figure 10.- Circumferential heat-transfer distribution. $\alpha = 90^0$.

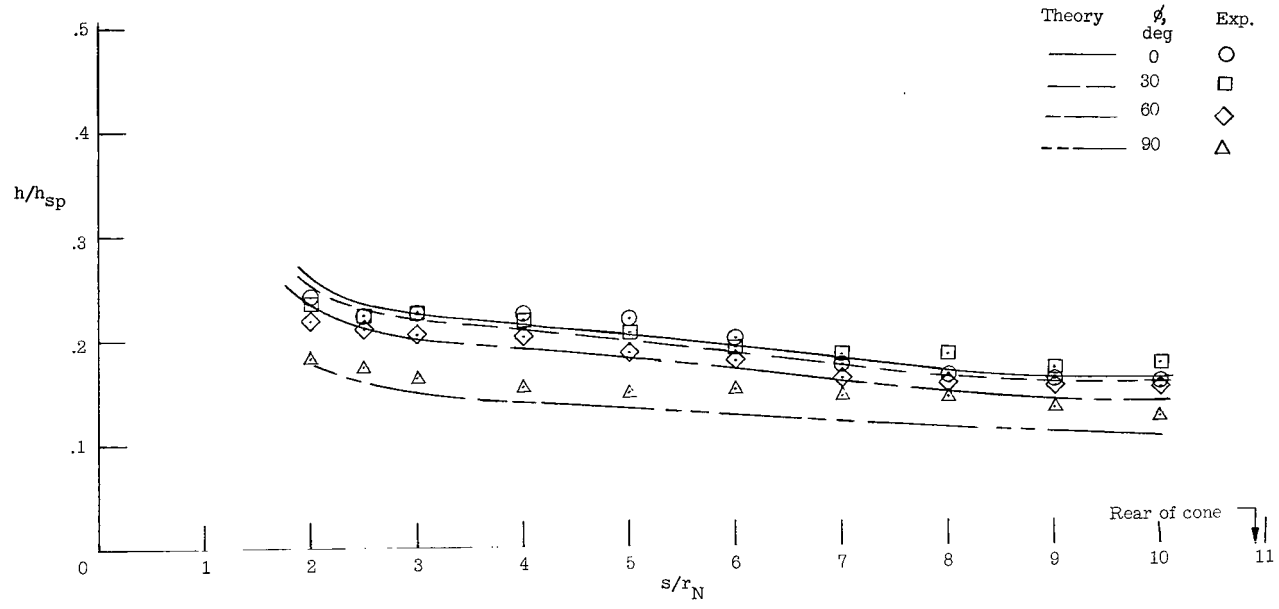

(a) $R_{\infty,d} = 0.37 \times 10^6$.

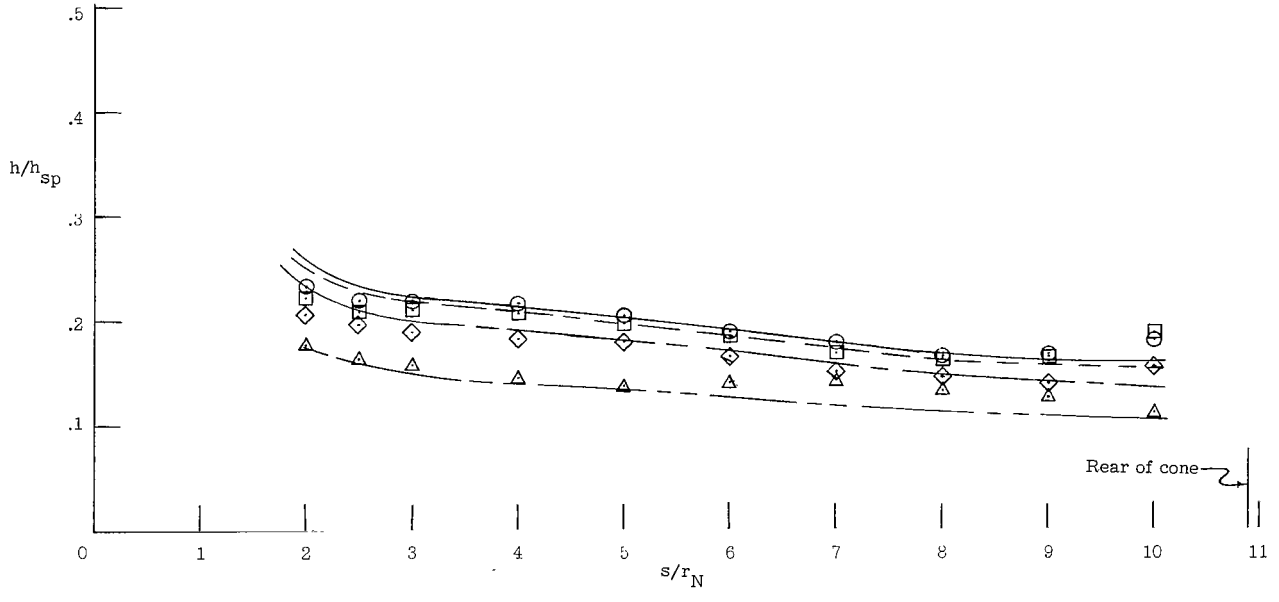

(b) $R_{\infty,d} = 1.65 \times 10^6$.

Figure 11.- Heat-transfer distributions over 25^0 half-angle spherically blunted cone. $\alpha = 5^0$.

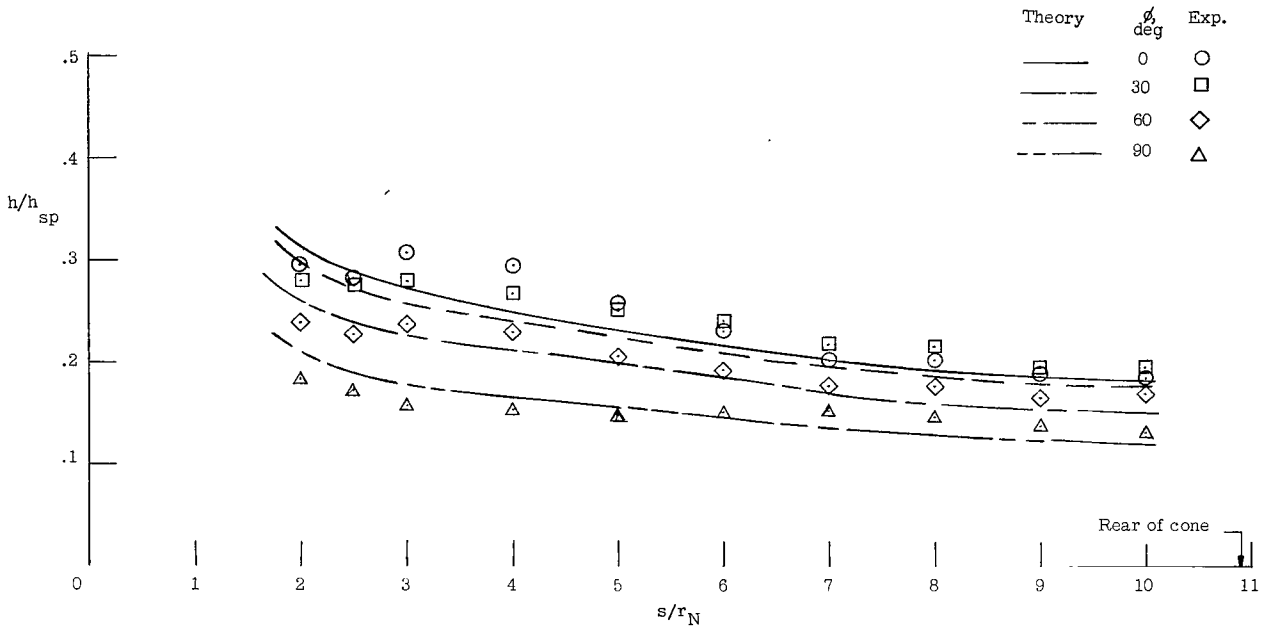

(a) $R_{\infty,d} = 0.37 \times 10^6$.

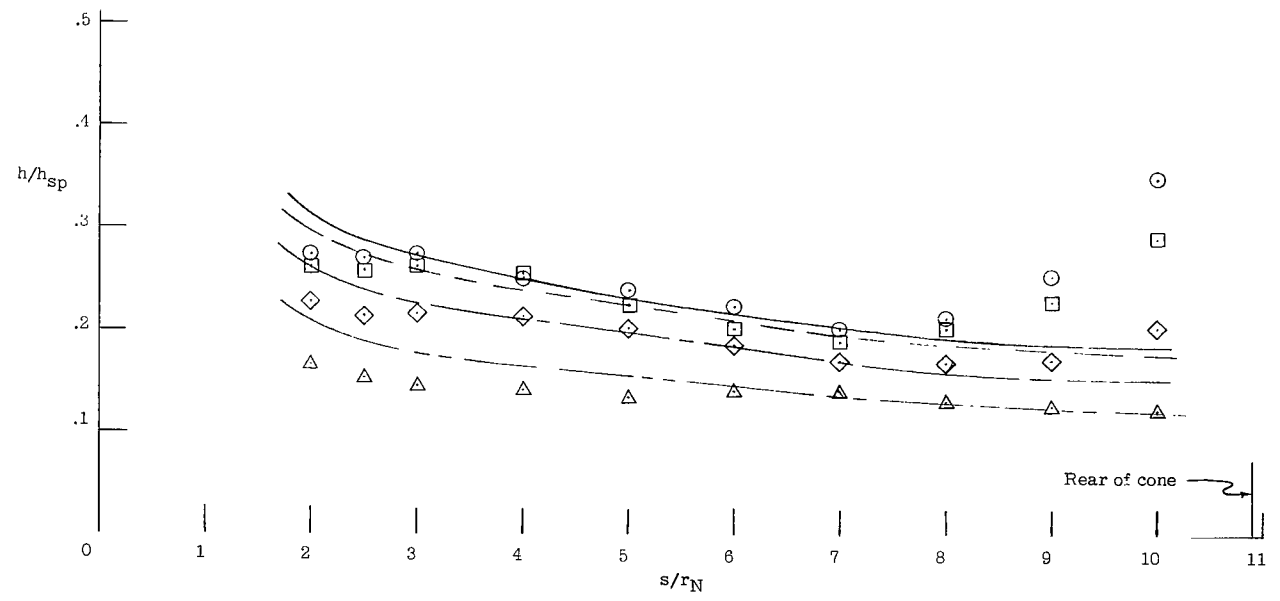

(b) $R_{\infty,d} = 1.65 \times 10^6$.

Figure 12.- Heat-transfer distributions over 25° half-angle spherically blunted cone. $\alpha = 10^0$.

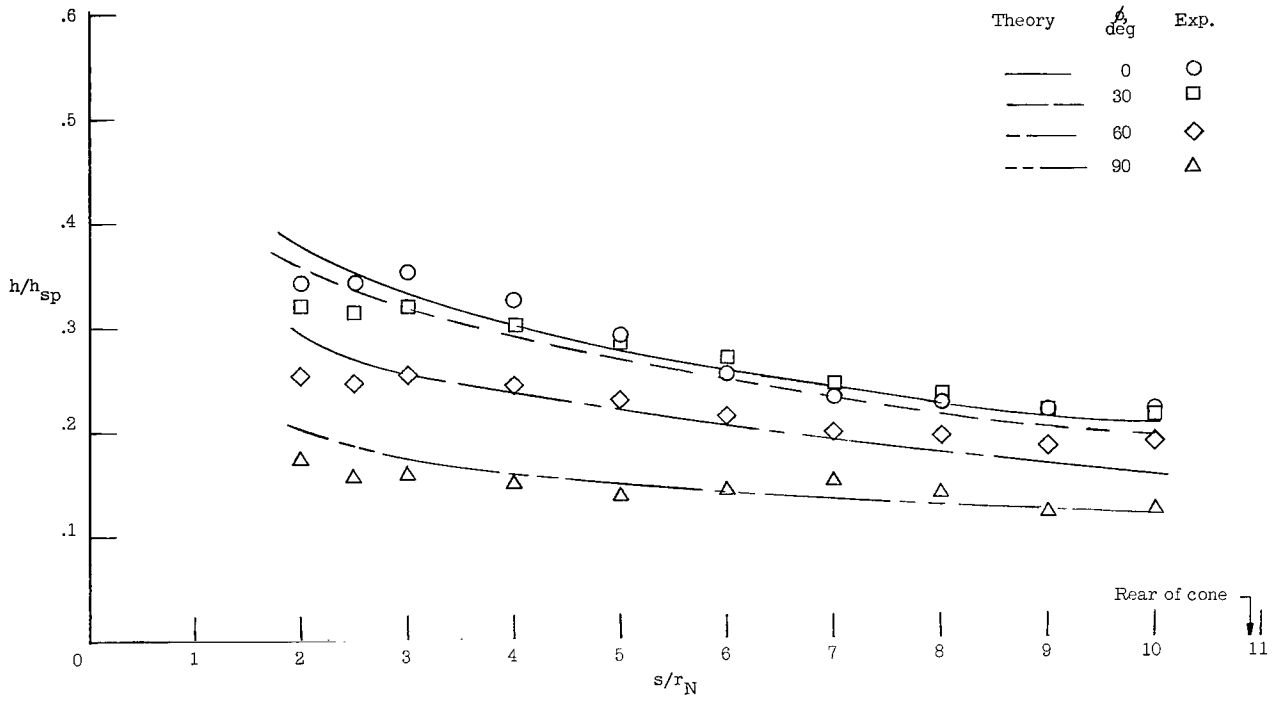

(a) $R_{\infty,d} = 0.37 \times 10^6$.

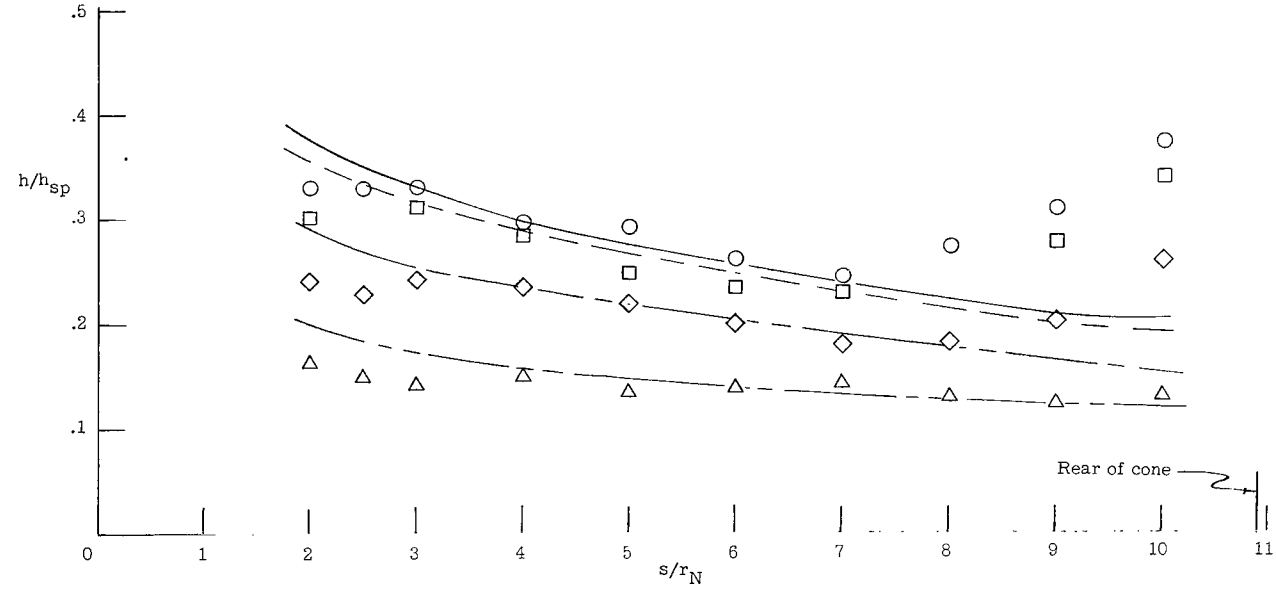

(b) $R_{\infty,d} = 1.65 \times 10^6$.

Figure 13.- Heat-transfer distribution over 25° half-angle spherically blunted cone. $\alpha = 15°$.

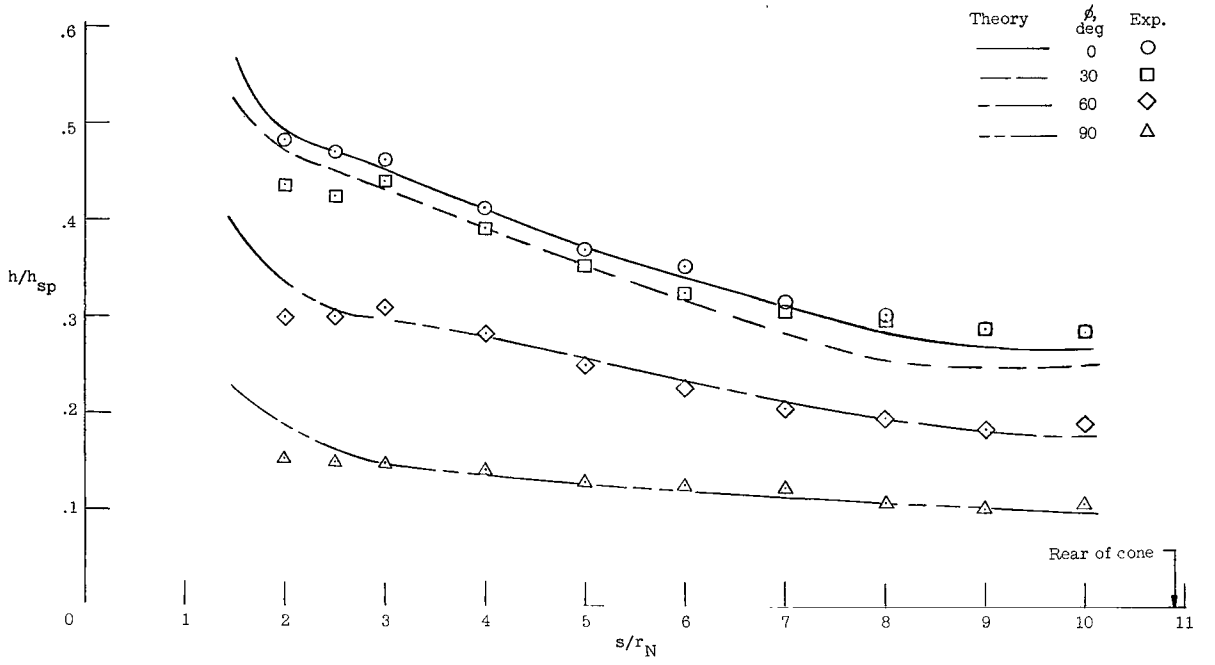

(a) $R_{\infty,d} = 0.37 \times 10^6$.

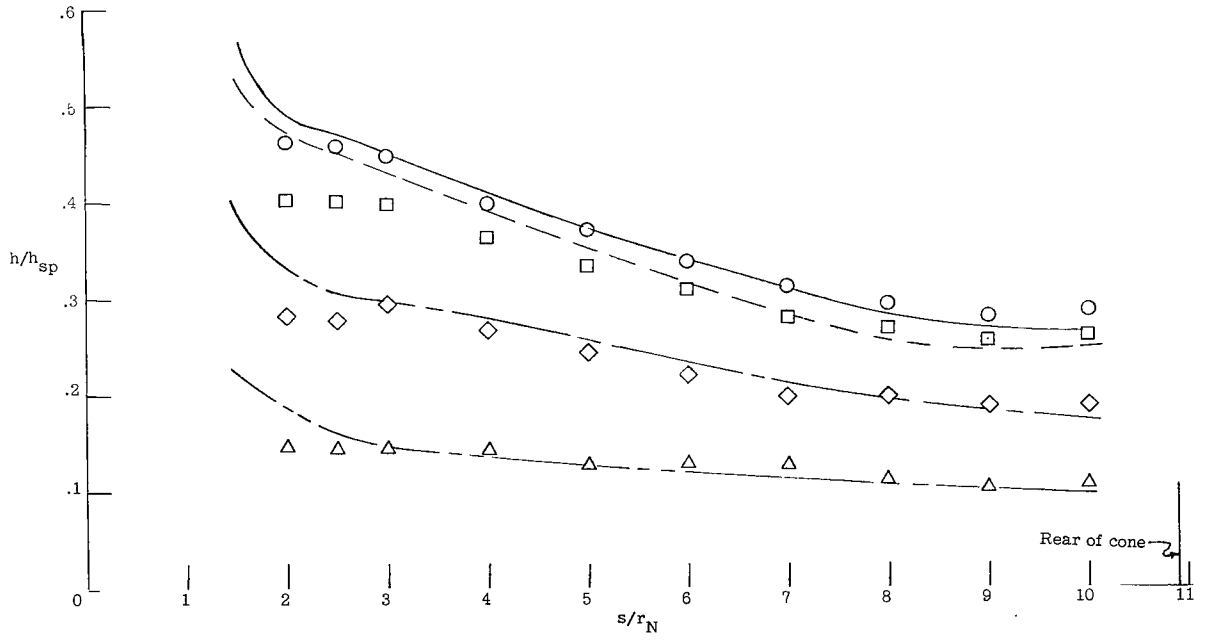

(b) $R_{\infty,d} = 1.65 \times 10^6$.

Figure 14.- Heat-transfer distribution over 25^0 half-angle spherically blunted cone. $\alpha = 30^0$.

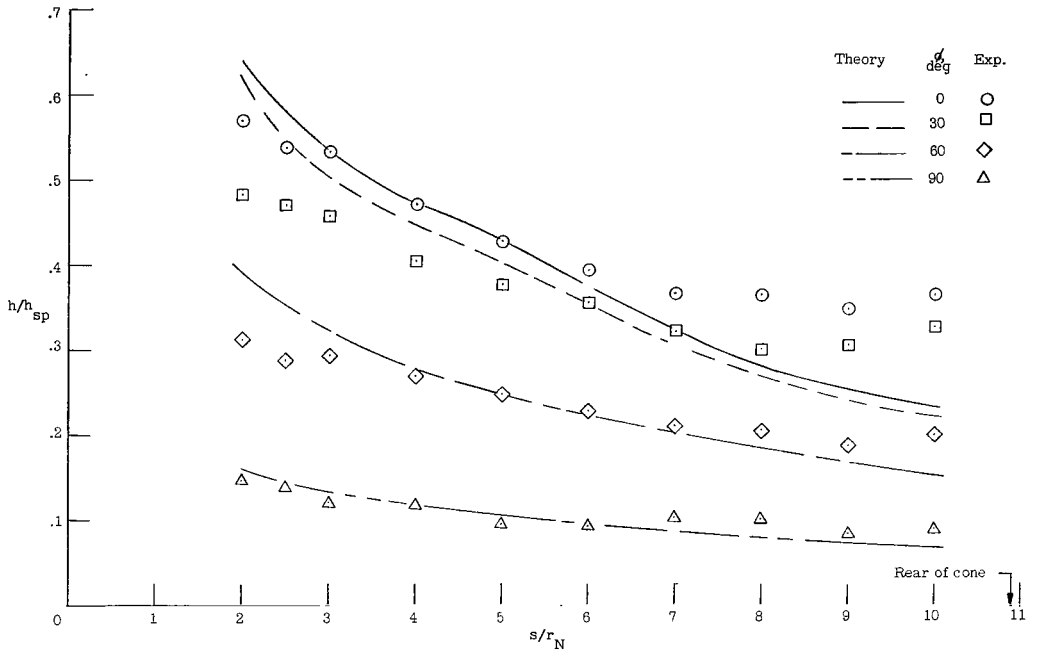

(a) $R_{\infty,d} = 0.37 \times 10^6$.

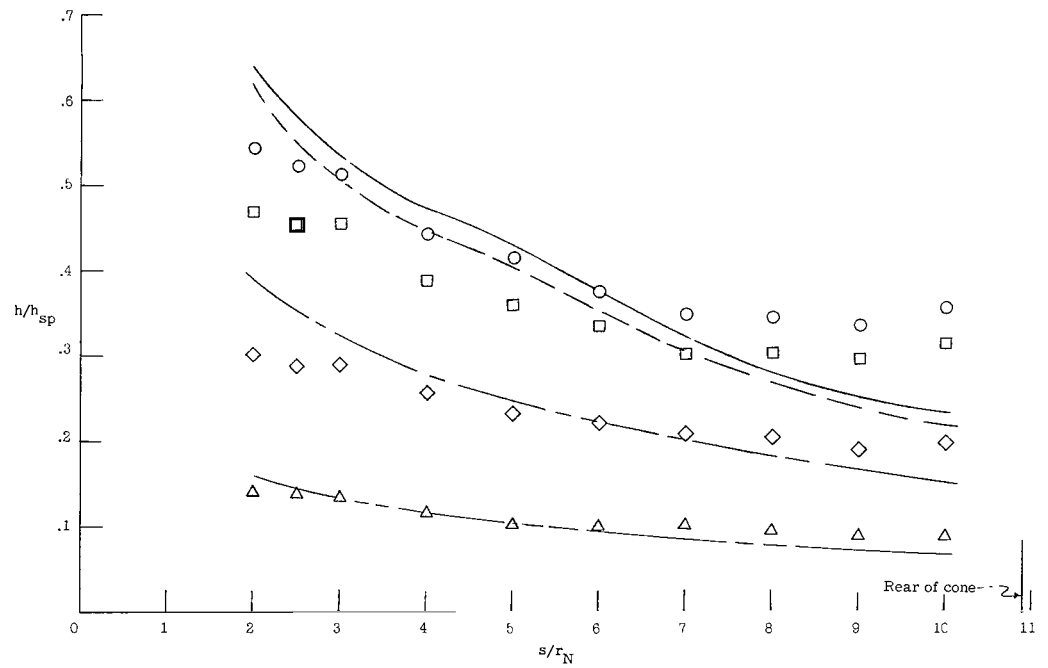

(b) $R_{\infty,d} = 1.65 \times 10^6$.

Figure 15.- Heat-transfer distribution over 25° half-angle spherically blunted cone. $\alpha = 45°$.

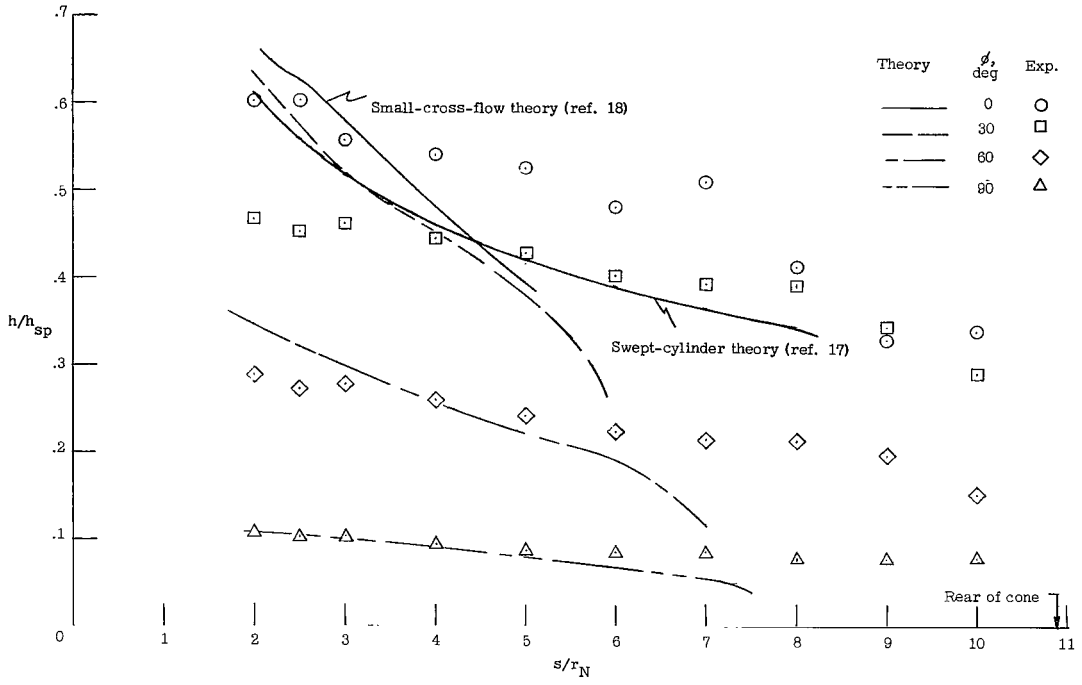

(a) $R_{\infty,d} = 0.37 \times 10^6$.

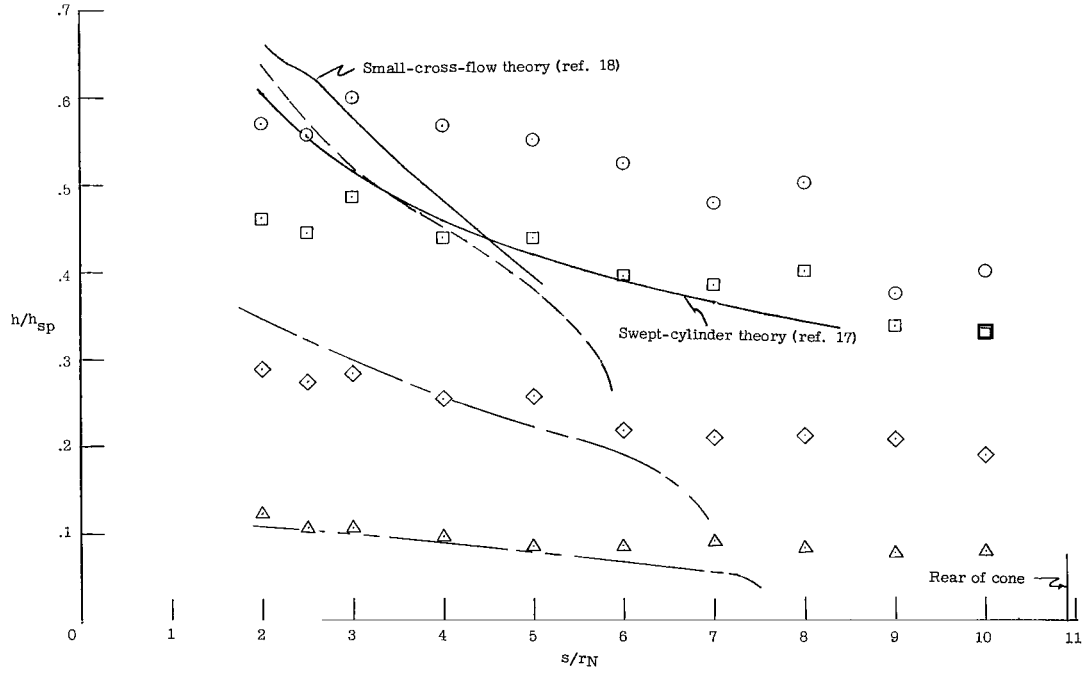

(b) $R_{\infty,d} = 1.65 \times 10^6$.

Figure 16.- Heat-transfer distribution over 25° half-angle spherically blunted cone. $\alpha = 60^0$.

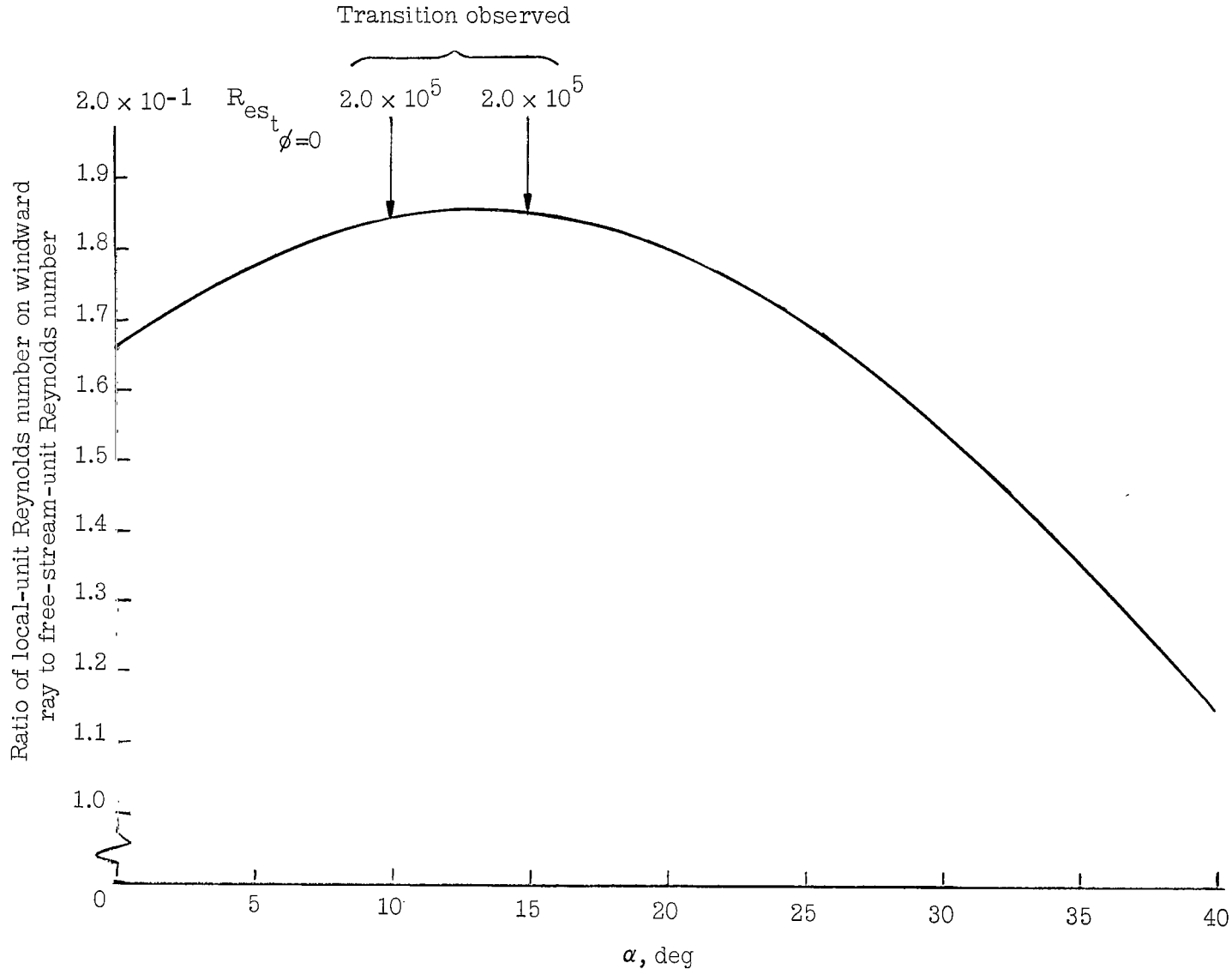

Figure 17.- Variation of local-external-unit Reynolds number with angle of attack along windward ray of conical surface.

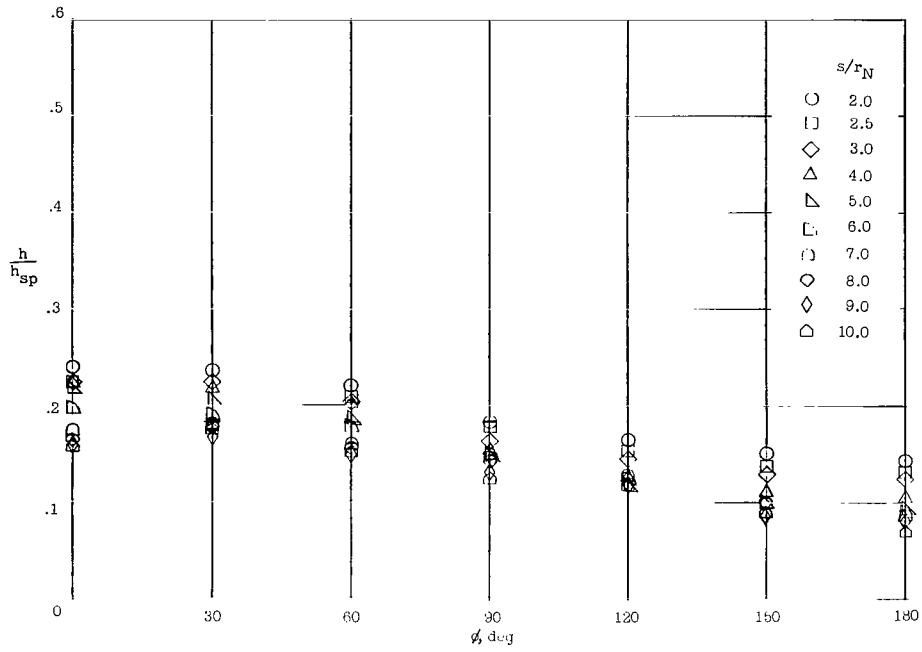

(a) $R_{\infty,d} = 0.37 \times 10^6$; $\alpha = 5^0$.

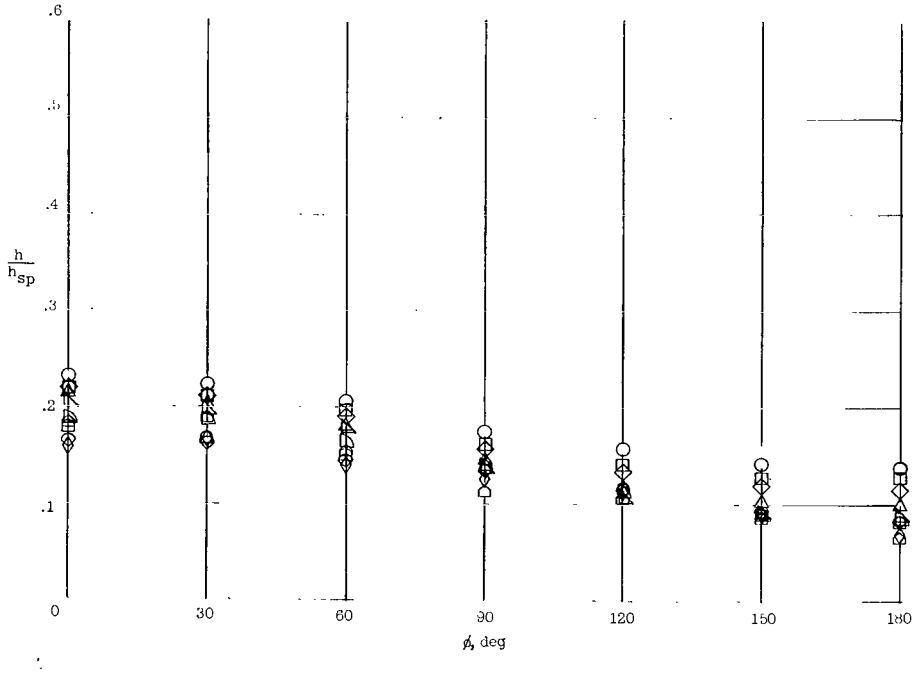

(b) $R_{\infty,d} = 1.65 \times 10^6$; $\alpha = 5^0$.

Figure 18.- Chordwise heat-transfer distribution over conical afterbody.

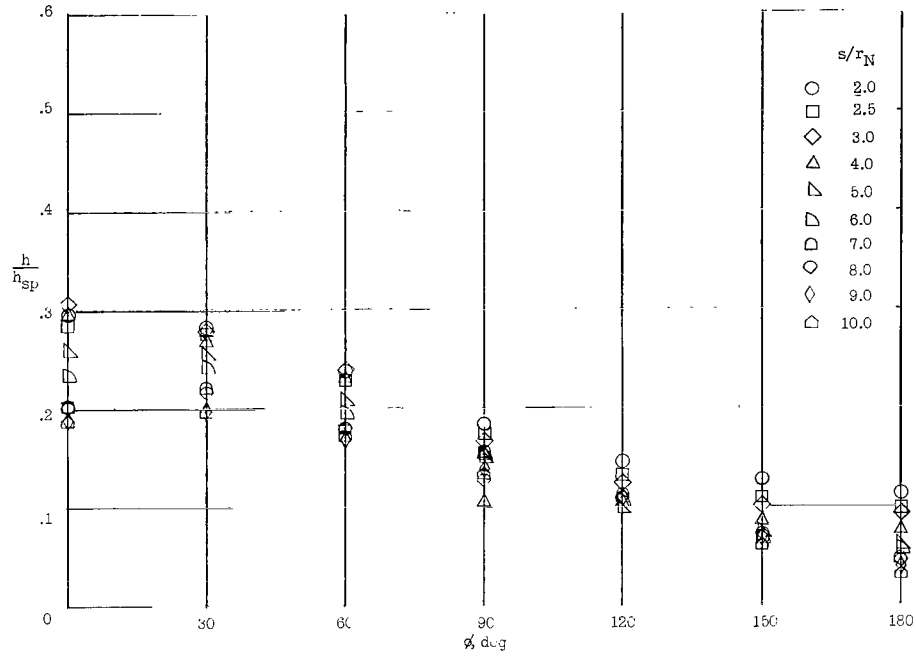

(c) $R_{\infty,d} = 0.37 \times 10^6$; $\alpha = 10^0$.

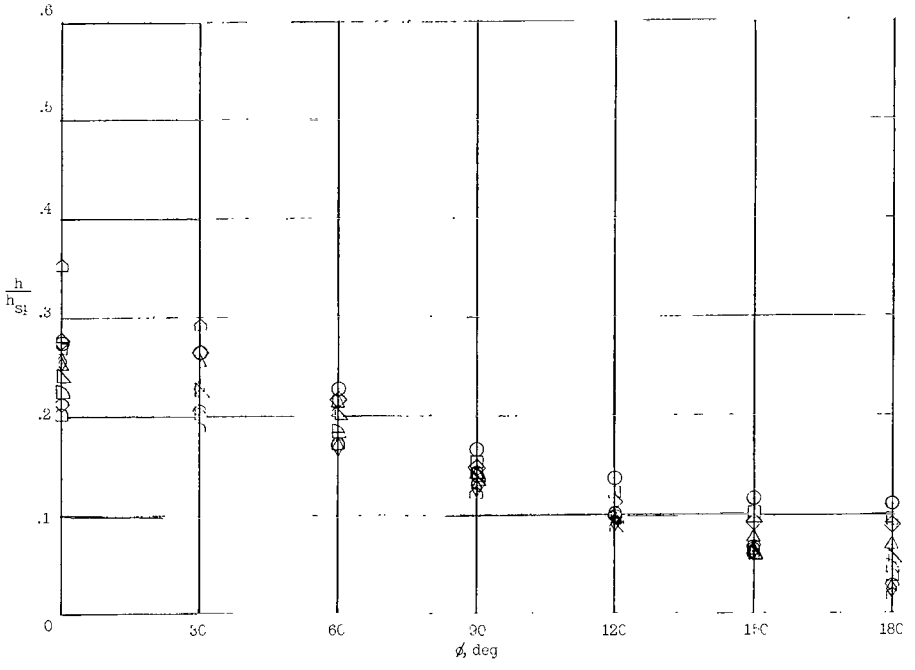

(d) $R_{\infty,d} = 1.65 \times 10^6$; $\alpha = 10^0$.

Figure 18.- Continued.

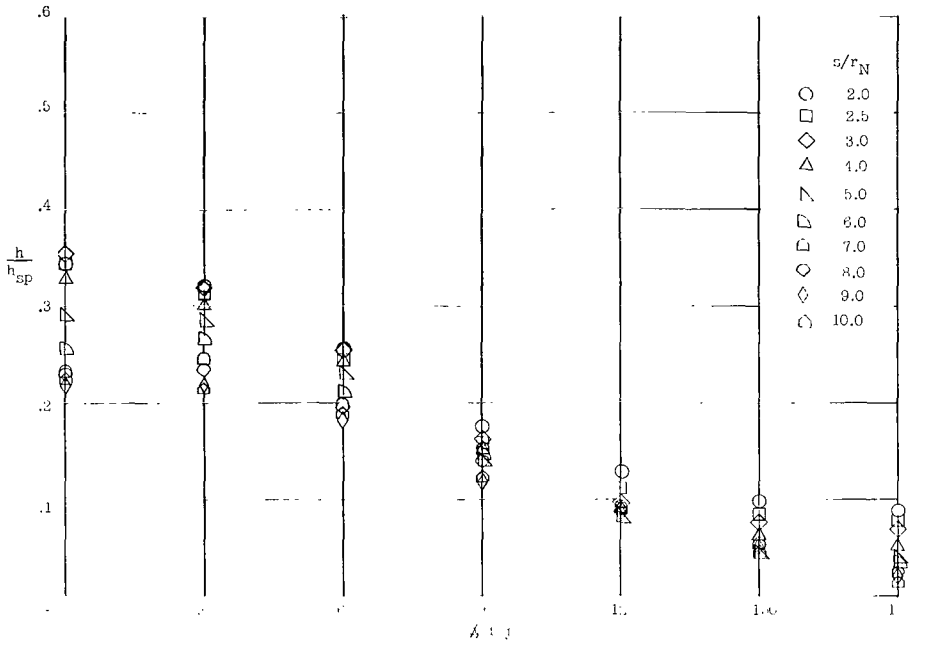

(e) $R_{\infty,d} = 0.37 \times 10^6$; $\alpha = 15^0$.

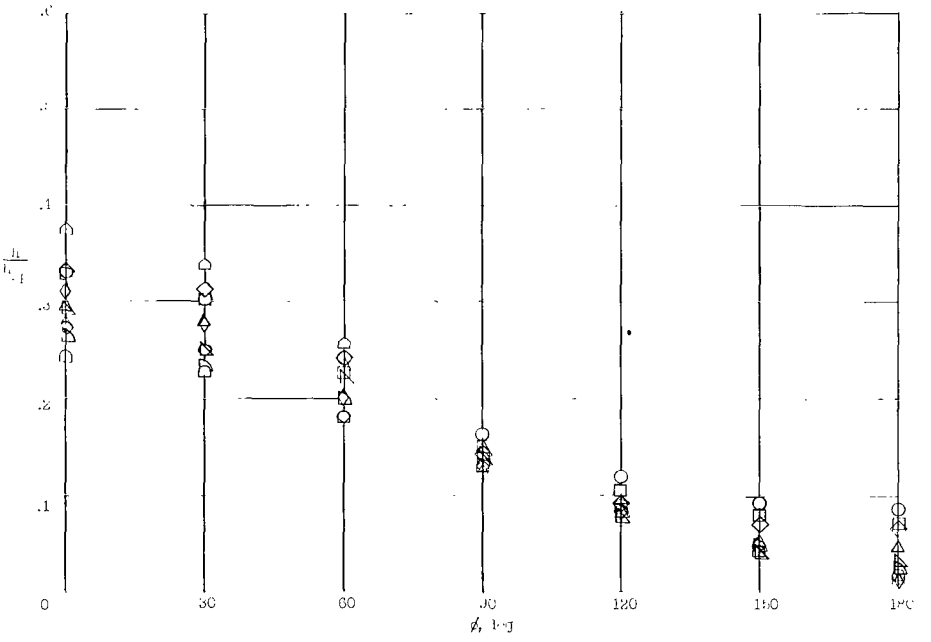

(f) $R_{\infty,d} = 1.65 \times 10^6$; $\alpha = 15^0$.

Figure 18.- Continued.

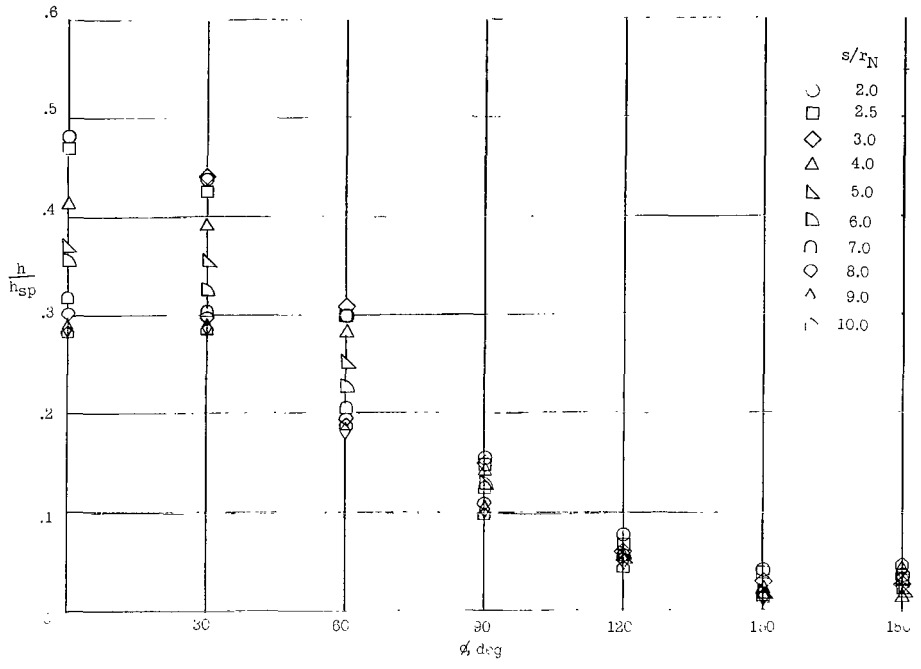

(g) $R_{\infty,d} = 0.37 \times 10^6$; $\alpha = 30^0$.

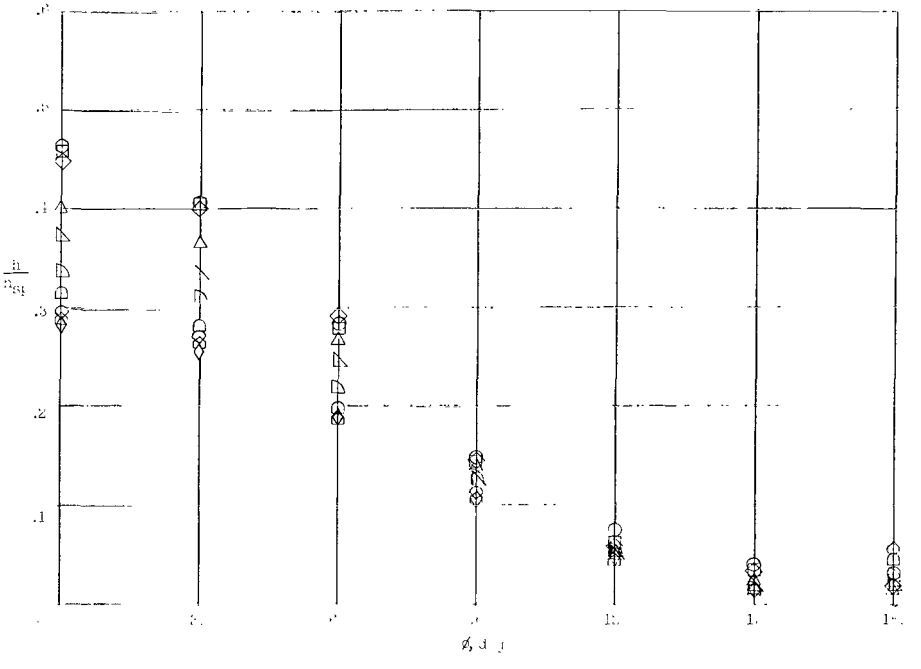

(h) $R_{\infty,d} = 1.65 \times 10^6$; $\alpha = 30^0$.

Figure 18.- Continued.

(i) $R_{\infty,d} = 0.37 \times 10^6$; $\alpha = 45^o$.

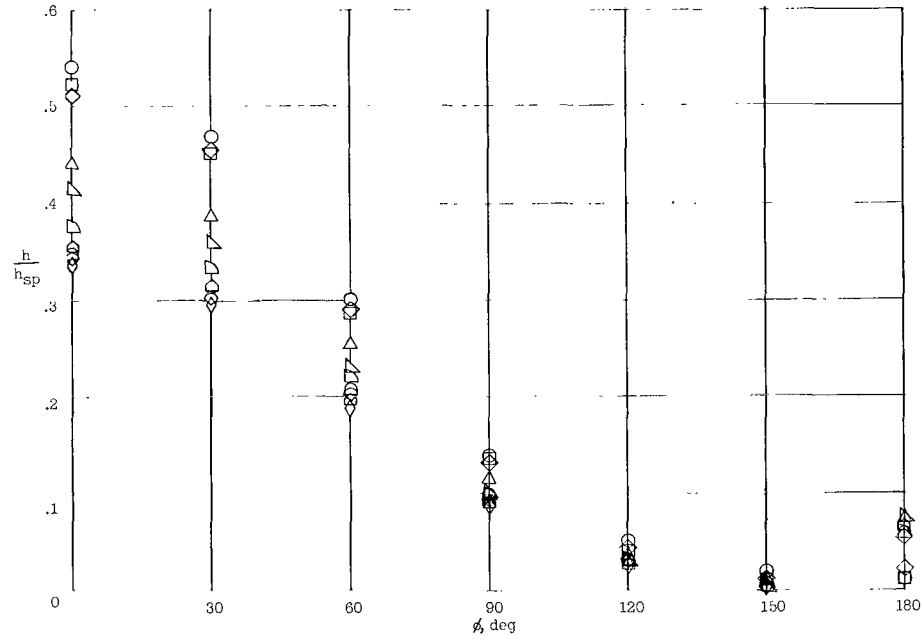

(j) $R_{\infty,d} = 1.65 \times 10^6$; $\alpha = 45^o$.

Figure 18.- Continued.

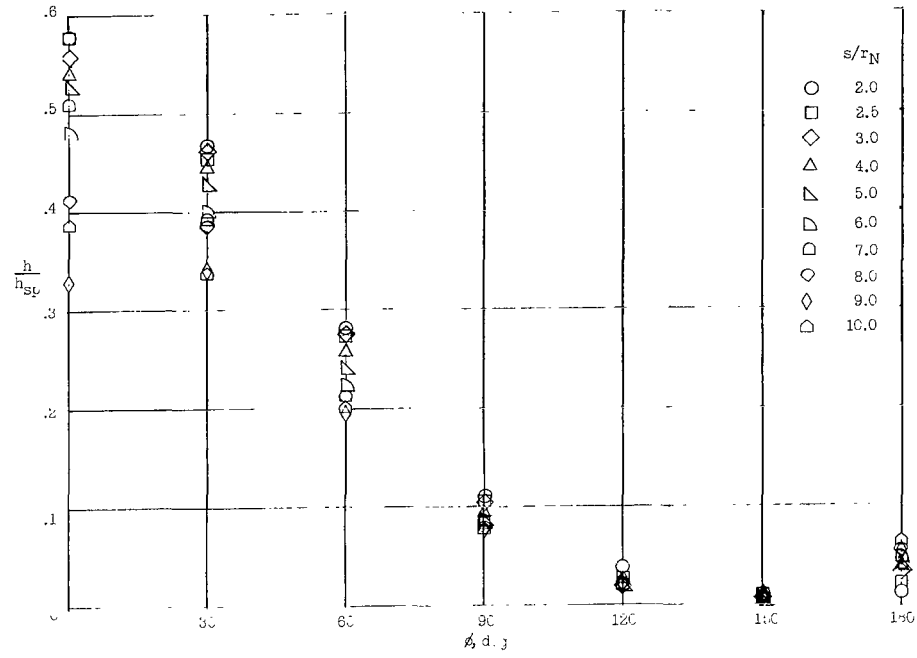

(k) $R_{\infty,d} = 0.37 \times 10^6$; $\alpha = 60^0$.

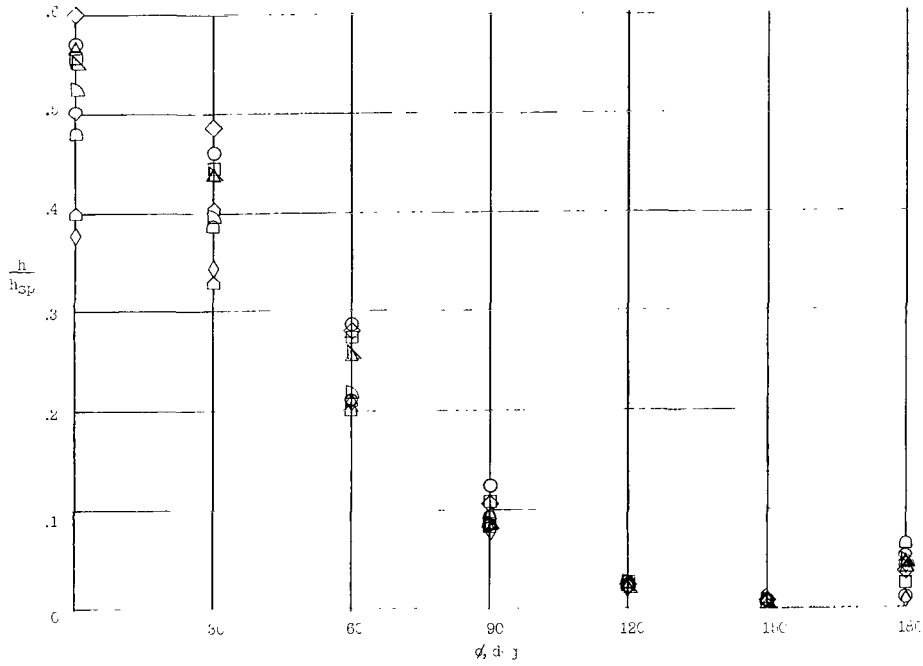

(l) $R_{\infty,d} = 1.65 \times 10^6$; $\alpha = 60^0$.

Figure 18.- Concluded.

NASA-Langley, 1968 — 1 L-5935